Elsevier Editorial System(tm) for Lithos
Manuscript Draft

Manuscript Number: LITHOS7138R1

Title: Shallow forearc mantle dynamics and geochemistry: new insights from the IODP expedition 366

Article Type: Regular Article

Keywords: forearc, serpentinites, phase transition, dynamic, geochemistry, subduction zones

Corresponding Author: Dr. Baptiste Debret,

Corresponding Author's Institution: Université Libre de Bruxelles

First Author: Baptiste Debret

Order of Authors: Baptiste Debret; Elmar Albers; Bastien Walter; Roy Price; Jaime Barnes; Hugues Beunon; Sebastien Facq; David Gillikin; Nadine Mattielli; Helen Williams

Abstract: The Mariana forearc is a unique setting on Earth where serpentinite mud volcanoes exhume clasts originating from depths of 15 km and more from the forearc mantle. These peridotite clasts are variably serpentinized by interaction with slab derived fluid, and provide a record of forearc mantle dynamics and changes in geochemistry with depth. During International Oceanic Discovery Program (IODP) Expedition 366, we recovered serpentinized ultramafic clasts contained within serpentinite muds of three different mud volcanoes located at increasing distance from the Mariana trench and at increasing depth to the slab/mantle interface: Yinazao (distance to the trench: 55 km / depth to the slab/mantle interface: 13km), Fantangisña (62 km / 14 km) and Asùt Tesoru (72 km / 18 km). Four different types of ultramafic clasts were recovered: blue serpentinites, lizardite-serpentinites, antigorite/lizardite- and antigorite-serpentinites. Lizardite-serpentinites are primarily composed of orange serpentine, forming mesh and bastite textures. Raman and microprobe analyses revealed that these textures contain a mixture of Fe-rich brucite (XMg ~ 0.84) and lizardite/chrysotile. Antigorite/lizardite- and antigorite-serpentinites record the progressive recrystallization of mesh and bastite textures to antigorite, magnetite and pure Fe-poor brucite (XMg ~ 0.92). Oxygen isotope compositions of clasts and pore fluids showed that the transition from lizardite to antigorite is due to the increase in temperature from 200°C to about 400°C within the forearc area above the slab/mantle interface. Lizardite-, antigorite/lizardite- and antigorite-serpentinites displayed U-shaped chondrite normalized Rare Earth Element (REE) patterns and are characterized by high fluid mobile element concentrations (Cs, Li, Sr, As, Sb, B, Li) relative to abyssal peridotites and/or primitive mantle. The recrystallization of lizardite to antigorite is accompanied by a decrease in Cs, Li and Sr, and an increase in As and Sb concentrations in the bulk clasts, whereas B concentrations are relatively constant. Some clasts are overprinted by blue serpentine, often in association with sulfides. Most of these blue serpentinites were recovered at Yinazao and the uppermost units of Fantangisña and Asùt Tesoru suggesting alteration in the shallower portions of the forearc, possibly during exhumation of

the clasts. This episode of alteration resulted in a flattening of REE spectra and an increase of Zn concentrations in serpentinites. Otherwise, no systematic changes of ultramafic clasts chemistry or mineralogy were observed with increasing depth to the slab. The samples document previously undescribed prograde metamorphic events in the shallow portions of the Mariana subduction zone, consistent with a continuous burial of the serpentinized forearc mantle during subduction. Similar processes, induced by the interaction with fluids released from the downgoing slab, likely occur in subduction zones worldwide. At greater depth, breakdown of brucite and antigorite will result in the massive transfer of fluids and fluid mobile elements, such as As, Sb and B, to the source of arc magmas.

Research Data Related to this Submission

There are no linked research data sets for this submission. The following reason is given:
Data are already provided in the article and the appendixes.

Abstract

The Mariana forearc is a unique setting on Earth where serpentinite mud volcanoes exhume clasts originating from depths of 15 km and more from the forearc mantle. These peridotite clasts are variably serpentinized by interaction with slab derived fluid, and provide a record of forearc mantle dynamics and changes in geochemistry with depth. During International Oceanic Discovery Program (IODP) Expedition 366, we recovered serpentinized ultramafic clasts contained within serpentinite muds of three different mud volcanoes located at increasing distance from the Mariana trench and at increasing depth to the slab/mantle interface: Yinazao (distance to the trench: 55 km / depth to the slab/mantle interface: 13km), Fantangisña (62 km / 14 km) and Asùt Tesoru (72 km / 18 km). Four different types of ultramafic clasts were recovered: blue serpentinites, lizardite-serpentinites, antigorite/lizardite- and antigorite-serpentinites. Lizardite-serpentinites are primarily composed of orange serpentine, forming mesh and bastite textures. Raman and microprobe analyses revealed that these textures contain a mixture of Fe-rich brucite (XMg ~ 0.84) and lizardite/chrysotile. Antigorite/lizardite- and antigorite-serpentinites record the progressive recrystallization of mesh and bastite textures to antigorite, magnetite and pure Fe-poor brucite (XMg ~ 0.92). Oxygen isotope compositions of clasts and pore fluids showed that the transition from lizardite to antigorite is due to the increase in temperature from 200°C to about 400°C within the forearc area above the slab/mantle interface. Lizardite-, antigorite/lizardite- and antigorite-serpentinites displayed U-shaped chondrite normalized Rare Earth Element (REE) patterns and are characterized by high fluid mobile element concentrations (Cs, Li, Sr, As, Sb, B, Li) relative to abyssal peridotites and/or primitive mantle. The recrystallization of lizardite to antigorite is accompanied by a decrease in Cs, Li and Sr, and an increase in As and Sb concentrations in the bulk clasts, whereas B concentrations are relatively constant. Some clasts are overprinted by blue serpentine, often in association with sulfides. Most of these blue serpentinites were recovered at Yinazao and the uppermost units of Fantangisña and Asùt Tesoru suggesting alteration in the shallower portions of the forearc, possibly during exhumation of the clasts. This episode of alteration resulted in a flattening of REE spectra and an increase of Zn concentrations in serpentinites. Otherwise, no systematic changes of ultramafic clasts chemistry or

mineralogy were observed with increasing depth to the slab. The samples document previously undescribed prograde metamorphic events in the shallow portions of the Mariana subduction zone, consistent with a continuous burial of the serpentinized forearc mantle during subduction. Similar processes, induced by the interaction with fluids released from the downgoing slab, likely occur in subduction zones worldwide. At greater depth, breakdown of brucite and antigorite will result in the massive transfer of fluids and fluid mobile elements, such as As, Sb and B, to the source of arc magmas.

***Highlights (for review)**

Highlights:

- Clasts from Mariana mud volcanoes record three different stages of serpentinization
- Transition lizardite to antigorite enhanced by an increase of temperature from 200 to 400°C
- Evidences for a continuous burial of the serpentinized forearc during subduction
- Phase transitions accompanied by a modification of trace element chemistry

Shallow forearc mantle dynamics and geochemistry: new insights from the IODP expedition 366

B. Debret[1,2*], E. Albers[3], B. Walter[4], R. Price[5], J. D. Barnes[6], H. Beunon[1], S. Facq[2], D.P. Gillikin[7], N. Mattielli[1], H. Williams[2].

1: Laboratoire G-Time, DGES, Université Libre de Bruxelles, ULB, CP 160/02, 1050 Brussels, Belgium

2: Department of Earth Sciences, University of Cambridge, Downing Street, Cambridge CB2 3EQ, UK

3: Department of Geosciences and MARUM – Center for Marine Environmental Sciences, University of Bremen, Germany

4: UMR-CNRS 7359 GeoRessources, ENSG - University of Lorraine, 2 rue du Doyen Marcel Roubault, 54518 Vandoeuvre-les-Nancy Cedex, France

5: Stony Brook University, SoMAS, Stony Brook, New York 11794, USA

6: Dept. of Geological Sciences, Jackson School of Geosciences, University of Texas, Austin, TX 78712, USA

7: Union College, Dept. of Geology, Schenectady, NY, 12308, USA

**: corresponding author (ba.debret@gmail.com)*

Abstract

The Mariana forearc is a unique setting on Earth where serpentinite mud volcanoes exhume clasts originating from depths of 15 km and more from the forearc mantle. These peridotite clasts are variably serpentinized by interaction with slab derived fluid, and provide a record of forearc mantle dynamics and changes in geochemistry with depth. During International Oceanic Discovery Program (IODP) Expedition 366, we recovered serpentinized ultramafic clasts contained within serpentinite muds of three different mud volcanoes located at increasing distance from the Mariana trench and at increasing depth to the slab/mantle interface: Yinazao (distance to the trench: 55 km / depth to the slab/mantle interface: 13km), Fantangisña (62 km / 14 km) and Asùt Tesoru (72 km / 18 km). Four different types of ultramafic clasts were recovered: blue serpentinites, lizardite-serpentinites, antigorite/lizardite- and antigorite-serpentinites. Lizardite-serpentinites are primarily composed of orange serpentine, forming mesh and bastite textures. Raman and microprobe analyses revealed that these textures contain a mixture of Fe-rich brucite (XMg ~ 0.84) and lizardite/chrysotile. Antigorite/lizardite- and antigorite-serpentinites record the progressive recrystallization of mesh and bastite textures to antigorite, magnetite and pure Fe-poor brucite (XMg ~ 0.92). Oxygen isotope compositions of clasts and pore fluids showed that the transition from lizardite to antigorite is due to the increase in temperature from 200°C to about 400°C within the forearc area above the slab/mantle interface. Lizardite-, antigorite/lizardite- and antigorite-serpentinites displayed U-shaped chondrite normalized Rare Earth Element (REE) patterns and are characterized by high fluid mobile element concentrations (Cs, Li, Sr, As, Sb, B, Li) relative to abyssal peridotites and/or primitive mantle. The recrystallization of lizardite to antigorite is accompanied by a decrease in Cs, Li and Sr, and an increase in As and Sb concentrations in the bulk clasts, whereas B concentrations are relatively constant. Some clasts are overprinted by blue serpentine, often in association with sulfides. Most of these blue serpentinites were recovered at Yinazao and the uppermost units of Fantangisña and Asùt Tesoru suggesting alteration in the shallower portions of the forearc, possibly during exhumation of the clasts. This episode of alteration resulted in a flattening of REE spectra and an increase of Zn concentrations in serpentinites. Otherwise, no systematic changes of ultramafic clasts chemistry or

mineralogy were observed with increasing depth to the slab. The samples document previously undescribed prograde metamorphic events in the shallow portions of the Mariana subduction zone, consistent with a continuous burial of the serpentinized forearc mantle during subduction. Similar processes, induced by the interaction with fluids released from the downgoing slab, likely occur in subduction zones worldwide. At greater depth, breakdown of brucite and antigorite will result in the massive transfer of fluids and fluid mobile elements, such as As, Sb and B, to the source of arc magmas.

Keywords: forearc, serpentinites, phase transition, dynamic, geochemistry, subduction zones

1. Introduction

Serpentinization of the forearc mantle in subduction zones is intimately related to the devolatilization of the downgoing slab. During the onset of subduction (i.e., less than ~80 km depth) volatiles, such as H_2O, C, S, etc., are released from the slab, rise through and interact with the mantle wedge. This process influences the physical and mechanical properties of the slab/mantle wedge interface (Gerya et al., 2002; Rüpke et al., 2004; Van Keken et al., 2011), the dynamics of mantle flows (Hilairet and Reynard, 2009; Reynard, 2013; Wada et al., 2008) and controls deep volatile and redox-sensitive element cycles (Debret et al., 2018a; Deschamps et al., 2011; Hattori and Guillot, 2007; Ribeiro and Lee, 2017; Savov et al., 2007, 2005). In addition, serpentinites, either in the slab and/or the mantle wedge, have the capability to retain large amounts of water (up to 13 wt%) down to 100-200 km and up to their transformation into chlorite bearing harzburgites (e.g., Ulmer and Trommsdorff, 1995; Wunder and Schreyer, 1997). However, despite its importance, relatively little is known about the extent of serpentinization, redox state and chemistry of serpentinized forearc mantle wedges worldwide.

A common way to study serpentinized forearc mantle wedges is by measuring seismic velocities (Bostock et al., 2002; Kamimura et al., 2002). Although the geometry of forearcs is highly variable and strongly controlled by the age of the slab (e.g., Van Keken et al., 2011; Reynard, 2013; Wada et al., 2008), it is widely assumed that the forearc mantle wedge is highly serpentinized, typically more

than 50 % (Bostock et al., 2002; Nagaya et al., 2016), at depth ranging from 30 to 80 km. The physical properties of the mantle wedge serpentinites are often approximated by the behaviour of antigorite (i.e., the high temperature and pressure form of serpentine). Both modelling and experimental studies suggest that antigorite should be the dominant phase crystallizing in the forearc mantle (e.g., Christensen, 2004), but the importance of other serpentine varieties (lizardite and/or chrysotile) and minerals such as brucite, talc or chlorite, is poorly constrained (Reynard, 2013).

The buoyancy of serpentinized peridotites in dense anhydrous peridotites has lead several studies to propose that the serpentinized forearc mantle (or the so-called "serpentinization channel" along the slab-wedge interface) may contribute to the exhumation of high pressure terranes in active subduction zones (e.g., Chemenda et al., 1995; Guillot et al., 2000; Schwartz et al., 2001). This conclusion has been supported by the common occurrence of serpentinites with eclogitic rocks in mountain ranges. However, geochemical studies have shown that the forearc mantle wedge constitutes an essential reservoir for fluid mobile elements and water in subduction zones that must be dragged down by corner flow to contribute to the elemental and isotope budgets of subduction zone magmas (e.g. Savov et al., 2005, 2007; Hattori and Guillot, 2007; Deschamps et al., 2011; Ribeiro and Lee, 2017; Debret et al., 2018a). For example, recent mass balance calculations show that the serpentinized fore-arc mantle could provide enough water (~7–78% of the total water injected at the trenches) to account for the water outfluxes beneath the volcanic arc (Ribeiro and Lee, 2017). Additionally, numerical models by Nagaya et al. (2016) suggest that convection could develop in serpentinized forearc mantle wedges. This result is compatible with previous numerical modelling by Honda et al. (2010) indicating that convective flow can be induced in the forearc wedge mantle when the viscosity of the wedge mantle is sufficiently low ($< \sim 4 \times 10^{19}$ Pa s^{-1}); compatible with estimates for the effective viscosity of antigorite (Hilairet et al., 2007). The discrepancies between these buoyancy and viscosity-controlled models emphasize the difficulty in assessing the dynamics of mantle flow in the serpentinized mantle wedge in subduction zones.

The Mariana forearc is a unique setting to sample and study the serpentinized mantle wedge as protrusions of hydrated mantle form serpentinite mud volcanoes on the outer forearc of the Izu–

Bonin–Mariana intra-oceanic subduction system (Fryer & Mottl, 1992; Fryer et al., 2012; Taylor & Smoot, 1984). The mud volcanoes are composed of serpentinite muds with embedded ultramafic clasts from the forearc mantle as well as mafic clasts from the subducting crust, originating from depths greater than 15 km (Fryer et al., 2000; Maekawa et al., 1993). Here we take advantage of the recent International Ocean Discovery Program (IODP) Expedition 366 to study serpentinized ultramafic clasts contained in the serpentinite muds of three mud volcanoes: Yinazao (formerly known as Blue Moon), Fantangisña (Celestial) and Asùt Tesoru (Big Blue; Fryer et al., 2018). We show that clasts from the Mariana forearc mantle are variably serpentinized and preserve various stages of lizardite recrystallization into antigorite, brucite and magnetite. Oxygen isotope chemistry and thermometry of the clasts and pore fluids show that the transition from lizardite to antigorite is likely to occur between 200 to 400°C, in good agreement with thermodynamic calculations (Evans, 2004) and field observations in alpine meta-ophiolites (Schwartz et al., 2013). No obvious correlation between the distance of the mud volcanoes to the trench and the lizardite to antigorite transition was observed. The absence of correlation suggests that complex convective flows of material occur within the mantle wedge area.

2. Geological setting

The non-accretionary Mariana subduction system, involving the subduction of the Mesozoic Pacific plate below the Philippine Sea plate, is located in the Western Pacific Ocean (Fig. 1). At the surface, the Mariana forearc is characterised by multiple horst and graben structures that developed under extensional stress caused by a rapid slab roll-back (Fryer, 1996; Harry and Ferguson, 1991). As a result, numerous serpentinite mud volcanoes are situated at varying distances from the trench (Fig. 1). They are formed by the eruption of mud flows consisting of unconsolidated serpentinite mud and containing variably serpentinized ultramafic clasts, as well as minor amounts of recycled Pacific plate and of Philippine Sea plate materials (Fryer et al., 2018; Fryer, 2012; Maekawa et al., 1993; Pabst et al., 2011). The serpentinite muds are derived from the forearc mantle where slab derived fluids interact with ultramafic lithologies and are buoyantly transported to the seafloor (Fryer, 2012 and reference therein). IODP Expedition 366 drilled at Yinazao (formerly known as Blue Moon), Fantangisña

(Celestial) and Asùt Tesoru (Big Blue) serpentinite mud volcanoes, which are located at distances of 55 km, 65 km and 70 km to the trench, respectively. Two additional serpentinites mud volcanoes, namely South Chamorro (78 km) and Conical (86 km from the trench), were previously drilled during Ocean Drilling Leg 195 and 125, respectively, and data from these sites will be incorporated here.

Yinazao is the closest to the trench. It lies at 15°43'N latitude and 147°11'E longitude (Fig. 1), at about 13 km above the subducting slab (Fryer et al., 2018; Hulme et al., 2010; Oakley, 2008). Previous studies estimated the temperature of the slab/ mantle interface below Yinazao at about 80°C (Oakley, 2008; Hulme et al., 2010). Drilling took place at the flank (Site U1491) and the summit (Site U1492) of this mud volcano (Fryer et al., 2018). The recovered cores consisted mainly of an alternation of an uppermost altered units of red-brown pelagic mud, ranging from a few cm to up to 4 m thick, and units of green and blue-grey serpentinite pebbly mud (Fig. 2). The red-brown pelagic units are interpreted as paleo-seafloor horizons altered in contact with seawater between two mud eruptions (Fryer et al., 2018). Each unit contains between 5 and 10% ultramafic clasts, most of which are fully serpentinized. Clasts recovered from the upper unit are affected by brown weathering and can display a high degree of carbonation (up to 80%, Figs 2a-b, Appendix A); whereas, clasts from the lower units are characterised by a dark blue colour (Figs 2c-d) and are frequently crosscut by mm-wide chrysotile veins with crack-seal like textures, indicative of a late-stage alteration event.

Fantangisña mud volcano is located to the north of Yinazao, at approximately 16°32'N and 147°13'E (Fig. 1). It is situated at about 14 km above the slab (Hulme et al., 2010). The temperature of the slab/ mantle interface below Fantangisña mud-volcano was estimated at about 150°C (Fryer et al., 2018; Hulme et al., 2010). During IODP Expedition 366, both the summit (Site U1497) and the flank (Site U1498) of this mud volcano were drilled (Fryer et al. 2018). The recovered cores consisted of alternating silt- or sand-rich layers containing ultramafic clasts with a brown weathering colour, and of green and/or blue-grey serpentinite pebbly mud embedding a large amount (about 20%) of dark blue ultramafic clasts (Figs 2c-d) that are predominantly harzburgites and dunites displaying a wide degree of serpentinization degree, from about 50 to 100%.

Asùt Tesoru mud volcano lies to the north of Fantangisña, at approximately 18°06 N and 147.06 E (Fig. 1). It is located at about 18 km above the slab (Hulme et al., 2010). Temperatures at the slab/mantle interface are estimated at about 250°C (Fryer et al., 2018; Hulme et al., 2010). Three sites were drilled on the flanks (Sites U1493, U1494 and U1495) and one at the summit (Site U1496; Fryer et al., 2018). The uppermost recovered units consist of pelagic mud and fine grained sandstone or siltstone containing weathered ultramafic clasts. Lower units are mainly composed of green to blue-grey serpentinite mud with 2 to 15% lithic clasts mainly consisting of variably serpentinized harzburgites and dunites with a dark blue colour (Figs 2c-d; serpentinization degree from 30 to 100%).

3. Petrology of the ultramafic clasts

Forty three ultramafic clasts were examined for their petrography onshore (see Appendix B for sample IODP full names, locations and classification). The clasts are variably serpentinized harzburgites and dunites of several centimetres to tens of centimetres long (Fig. 2). Many clasts preserve different serpentinization stages reflecting various episodes of fluid infiltration within the mantle wedge.

3.1 Identification of serpentine varieties

The mineralogy of the ultramafic clasts was characterized by combining electron microprobe analyses and Raman spectroscopy. These methods have been used to differentiate between serpentine varieties and co-existing brucite (e.g., Debret et al., 2013; Groppo et al., 2006; Schwartz et al., 2013; Schwarzenbach et al., 2016). *In situ* major element analyses were performed with a CAMECA SX 100 electron microprobe at the Laboratoire Magmas et Volcans (Clermont-Ferrand, France). Operating conditions of 15 kV accelerating voltage, a sample current of 15 nA and a counting time of 10 s/element were used, except for Ni (20 s). Microprobe analyses are given in Appendix C. Raman spectroscopy was performed at the University of Cambridge (UK). Raman spectra were collected in the 150–1300 cm^{-1} and 3500-3800 cm^{-1} spectral ranges using a confocal Labram HR300 Raman spectrometer (Horiba Jobin Yvon) of 300 mm focal length equipped with a holographic grating of 1800 gr mm^{-1} coupled to a Peltier cooled front illuminated CCD detector, 1024×256 pixels in size. This configuration allowed for a spectral resolution of about 1.4 cm^{-1} per pixel. The excitation line at

532 nm was produced by a diode-pumped solid state laser (Laser Quantum) focused on the sample using an Olympus 50 X objective (0.42 N.A.). Spectra were corrected from a linear baseline using the fitting software Peakfit. The laser power was set at energies ranging from 5 mW to 500 µW in order to avoid degradation of serpentine or oxide minerals (Debret et al., 2013; Debret et al., 2014; Faria & Vena, 1997), and the sample surface was checked after each analysis. In order to properly define the different serpentine varieties, spectra of lizardite, chrysotile, antigorite and brucite were selected as references (Appendix D).

3.2 Serpentinization at Yinazao mud volcano

Close to the seafloor, the clasts mainly consisted of carbonated breccia made of dusty calcite and/or aragonite embedding serpentinite fragments of various sizes, from 100 µm to several centimetres (Figs 2a-b, 3a). The degree of carbonation varies from 20 to 80% in the different clasts. Serpentine minerals display pseudomorphic mesh and bastite textures that replace mantle olivines and orthopyroxenes, respectively. Large veins of chrysotile with crack seal like textures crosscut mesh and bastite textures. The rims of many clasts are affected by an episode of late alteration, consisting of brownish clay minerals, that overprints previous textures (Fig. 2b; Appendix A). This late alteration stage is in accordance with results from other studies on Conical and South Chamorro mud volcanoes drilled during previous ODP expeditions (e.g., Kahl et al., 2015).

In the deeper units, clasts consist mainly of blue serpentine, spinel and sulfides with rare hydrogrossular and relicts of mantle olivine and orthopyroxene (subsequently called 'blue serpentinites'; Figs 3b-d). Spinels are homogeneous and display euhedral shapes. They can be surrounded by ≤ 50 µm wide coronas of magnetite. Spinel cores have XCr (Cr / [Cr + Al]) of 53-54 and XMg (Mg / [Fe + Mg]) of 54-57 (Fig. 4). Serpentine forms mesh and bastite textures, replacing olivine and orthopyroxene, and display a pale blue colour in plane polarized light (Figs 3b,c). The Raman spectra of blue serpentine are characterized by peaks at 225, 381, 525, 692, 1095 and 3697 cm^{-1} characteristic of chrysotile. Brucite is intergrown with chrysotile at the microscale as indicated by additional Raman peaks at 280, 440, 3643 and 3650 cm^{-1} (Fig. 3b). Blue serpentine compositions are characterized by XMg of 0.85 to 0.94, and SiO_2 and FeO contents ranging from 17.9 to 40.3 wt% and

from 4.2 to 11.3 wt%, respectively (Fig. 5). The most Si-rich analyses display a broad match to serpentine mineral stoichiometry, whereas regression analysis of the whole data set suggests variable proportions of Mg-Si-serpentine and Si-free, Fe-rich brucite endmembers (Fig. 5). The low Si analyses can be attributed to the presence of Fe-brucite at nanoscale, as this mineral has a low XMg (~0.84 as shown by regression analyses in Fig. 5a) relative to serpentine and does not incorporate silica (see also Kahl et al., 2015; Schwarzenbach et al., 2016). Bastite textures are occasionally associated with roundish hydrogrossular crystals of about 50 µm width. Several studies have reported the presence of hydrogrossular in different serpentinization environments and this has, in most cases, been attributed to an excess in Al during the final stages of serpentine growth after pyroxene (e.g., Beard et al., 2009).

The centre of mesh and bastite textures is often associated with large opaque aggregates of ~200 µm width (Figs 3b,c). These aggregates are composed of lamellar minerals associated with framboidal Fe-sulfides (pyrite), ranging in size from 0.5 to 2 µm, formed inside the intergranular porosity (Fig. 3d). Raman analyses of the lamellar minerals show three main peaks at 280, 440 and 3639 cm^{-1} corresponding to brucite, with four small additional peaks at 369, 521, 689 and 3689 cm^{-1} suggesting the presence of small amounts of serpentine (Fig. 3b). Occasionally, 50 to 200 µm wide veins consisting mainly of euhedral pyrite crosscut the serpentine textures (Fig. 3c).

3.3 Serpentinization at Fantangisña and Asùt Tesoru mud volcanoes

Clasts recovered from Fantangisña and Asùt-Tesoru mud volcanoes display similar textures to each other. Samples from the uppermost units are also affected by sub-surface alteration such as clay mineral crystallization and carbonation. However, in contrast to Yinazao, the formation of blue serpentine and sulfides was mainly observed close to the seafloor at Fantangisña and Asùt Tesoru. The Blue serpentine can either completely replace former textures or be limited to clast rims (Fig. 2b; Appendix A). In lower units, three different types of ultramafic clasts have been identified (Figs 2c-d; 6-8); their distribution appears to be random within the mud volcanoes (see Appendix B for more details):

(1) The first group (lizardite-rich serpentinites, referred to as Liz-serpentinites from here on) corresponds to variably serpentinized peridotites that can preserve mantle minerals (olivine, orthopyroxene, spinel and rare clinopyroxene). These Liz-serpentinite clasts were the most commonly reported during previous ODP expeditions, i.e. in South Chamorro and Conical mud volcanoes (e.g., D'Antonio and Kristensen, 2004; Savov et al., 2005, 2007; Kahl et al., 2015). Olivine XMg and NiO contents range from 0.91 to 0.93 and from 0.37 to 0.44 wt%, respectively, whereas MnO contents are below 0.1 wt%. Orthopyroxene is characterized by Cr_2O_3 and Al_2O_3 contents ranging from 0.1 to 1.88 wt% and 0.1 to 0.5 wt%, respectively. Spinel relicts have euhedral shapes with dark cores and narrow (< 100 µm) lighter rims that correspond to a compositional zoning from Mg and Al-rich cores (XMg = 0.30 - 0.59; XCr = 0.51 – 0.95) to Cr-rich rims (XMg ~ 0; XCr ~ 1; Fig. 4). Small magnetite crystals are present at the boundary between serpentine and spinel. The serpentinization degrees of the clasts vary from about 30 to 90%. In slightly serpentinized clasts, serpentine crystallizes as brownish veins of 20 to 300 µm width, with regular shape, crossing olivine and orthopyroxene (Fig. 6a). Raman spectra indicate mixtures of brucite and lizardite and/or chrysotile inside the veins. Serpentine fully replaces olivine and orthopyroxene by forming mesh and bastite textures where the local serpentinization degree is > 60 %. No magnetite was observed in the mesh centres. Serpentine compositions are characterized by low SiO_2 (31.8 - 40.6 wt%), XMg (0.88 – 0.95) and high FeO (3.5 – 8.1 wt%; Fig. 5) suggesting variable proportions of Fe-brucite and serpentine at microscale. Bastite is associated with amphibole minerals, which form pale green needles about 50 µm in length. Rare magnetite grains have been observed in these clasts; they crystallize mainly in the centre of brucite veins of 20 to 200 µm width crossing mantle minerals, lizardite veins, mesh or bastite textures (Fig. 6b). Towards the rims, the brucite + magnetite veins are surrounded by a corona of small antigorite lamellae, about 30 µm in length.

(2) The second group (antigorite-/lizardite-rich serpentinites, referred as Atg/Liz-serpentinites from here on) corresponds to highly serpentinized peridotites (serpentinization degree > 70%) displaying mesh and bastite textures associated with antigorite (Fig. 7). Few primary mantle spinel relicts have been observed. XMg and XCr of spinel range from 0.19 to 0.39 and from 0.63 to 0.81,

respectively. Spinel frequently displays thin, about 50 µm wide, coronas of chromite (XCr > 0.9) and magnetite toward the rim (Fig. 4). Serpentine mesh centres are often several hundred micrometres in size and characterised by a homogenous grey colour with weak birefringence and occasionally undulatory extinction. Raman spectra of the mesh and bastite textures denote mixtures between lizardite (or chrysotile) and antigorite, with pronounced peaks at 1044 and 3700 cm^{-1} and at 1100 and 3685 cm^{-1}, corresponding to antigorite and lizardite, respectively (Fig. 7a). The mesh rims are composed of antigorite needles associated with thin veinlets of pure brucite and magnetite in their centres (Fig. 7a). Chemical compositions of serpentine minerals are homogeneous throughout the samples. They are characterized by higher SiO_2 (39.8 – 45.4 wt%) and XMg (0.92-0.97) and lower FeO (1.9-5.2 wt%) relative to serpentine/brucite textures in the Liz-serpentinites (Fig. 5). This suggests the absence of brucite at microscale. The amount of antigorite is highly variable from one sample to another, varying from about 40 to 80 modal %. The serpentinites are crosscut by 200 to 500 µm wide veins of brucite and magnetite (Fig. 7b). Mesh and bastite textures in contact with these veins are recrystallized to antigorite lamellae and needles about 30 µm in length.

(3) The third group corresponds to antigorite-bearing serpentinites (Atg-serpentinites from here on) mainly made of antigorite lamellae, about 50 µm long, with interstitial brucite and magnetite (Fig. 8). The existence of antigorite bearing clasts have also been reported at Conical and South Chamorro mud volcanoes (e.g., Alt and Shanks, 2006; Murata et al., 2009). Antigorite have higher SiO_2 contents (42.2 - 44.9 wt%) and XMg (0.96-0.99) and lower FeO contents (1.2-3.2 wt%) relative to serpentine in the Liz- or Atg/Liz-serpentinites (Fig. 5). Brucite has crystallized as millimetre-sized patches containing euhedral magnetite grains about 200 µm in width (Fig. 8). Brucite has MgO and FeO contents ranging from 63.3 to 64.9 wt% and 9.7 to 9.9 wt%, respectively, and an average XMg of 0.92, which is significantly higher than that of the Fe-Brucite in Liz-serpentinites (XMg ~ 0.84, Fig. 5). The Atg-serpentinites are characterized by the presence of euhedral hydro-andradite crystals that display a diamond shape and contain numerous inclusions of magnetite. The crystallization of andradite in serpentinites has been observed in several settings (e.g. Frost, 1985) and can be attributed to a low silica activity during alteration (Frost & Beard, 2007). Magnetite is abundant throughout the samples.

4. Methods

4.1 Oxygen isotope geochemistry

4.1.1 Mineral separates

The oxygen isotope compositions of serpentine and magnetite mineral separates were measured at the University of Texas at Austin using a ThermoElectron MAT 253 mass spectrometer. Serpentinite samples were crushed and handpicked under a binocular microscope in order to visually assess mineral separate purity. In many samples, serpentine and magnetite were extensively intergrown and pure magnetite could not be separated, therefore most samples could not be confidently analysed for the $\delta^{18}O$ value of magnetite. Oxygen isotope ratios were determined on ~ 2.0 mg of mineral separates using the laser fluorination method of Sharp (1990). Standard UWG-2 ($\delta^{18}O_{garnet}$ = +5.8‰; Valley et al., 1995) and in-house standard Lausanne-1 ($\delta^{18}O_{quartz}$ = +18.1‰) were analysed to verify precision and accuracy. All $\delta^{18}O$ values are reported relative to SMOW, where the $\delta^{18}O$ value of NBS-28 is +9.7‰. The error on $\delta^{18}O$ values is ±0.1‰, based on the long-term average of standard analyses.

4.1.2 Pore fluids

Whole-round (WR) core samples were taken immediately after core sectioning on the deck for the subsequent extraction of interstitial (pore) water (IW). The length of the WR core taken for IW analyses varied from 10 cm in the upper units, to 40 cm in the deeper units where the volume of extracted IW was limited. Although this sacrificed a large amount of core material, this was the only way to get sufficient volume of pore fluids for the deeper samples, and only core sections which appeared to be highly homogenous were used. Typically one WR per section was collected between 0 and 10 mbsf, and 2 WR were selected every 10 m of depth from 10 mbsf to total depth of the core. Whole-round samples were processed in a nitrogen filled glove-bag after cooling in a refrigerator for about one hour. First the cored material was extruded from the core liner, then portions of the material that were potentially contaminated by seawater and sediment smearing were removed by scraping the core's outer surface with a spatula. For advanced piston (APC) cores about 0.5 cm of material from the outer diameter and the top and bottom faces was removed. In contrast, material recovered by

extended core barrel (XCB) coring required additional removal of material, and as much as two-thirds of the sediment was removed from each WR sample. The remaining inner core of uncontaminated material (~150–300 cm^3) was placed into a titanium squeezer (modified after Manheim and Sayles, 1974) and compressed using a laboratory hydraulic press to extract pore water, using a total pressure up to 30 MPa. Fluids extracted from the compressed sediment sample were filtered through a pre-washed Whatman No. 1 filter situated above a titanium mesh screen. Approximately 10-80 mL of IW, depending on the length of the WR being processed, was collected in acid-cleaned plastic syringes attached to the squeezing assembly and filtered again through a Gelman polysulfone disposable filter (0.45 µm). After extraction, the squeezer parts were thoroughly cleaned with shipboard water, rinsed with de-ionized water, and dried. Pore fluids were syringe filtered into small, pre-cleaned (acid washed), Nalgene plastic vials, capped and then immediately flash frozen in liquid nitrogen to prevent evaporation.

Samples were measured via a Thermo Gas Bench II connected to a Thermo Delta Advantage mass spectrometer in continuous flow mode at Union College (Schenectady, New York – sample analyses are displayed in Appendix E). Three inhouse laboratory standards were used for isotopic corrections, and to assign the data to the appropriate isotopic scale using linear regression. These standards were calibrated directly to VSMOW (0.0‰) and SLAP (-55.50‰). The inhouse standards have $\delta^{18}O$ values that range from -0.6‰ to -16.52‰. The combined uncertainty (analytical uncertainty) for $\delta^{18}O$ of IW samples is ± 0.02‰ (SMOW), based on 8 internal tap water standards over two analytical sessions.

4.2 Bulk rock major and trace elements analyses

A suite of 25 representative serpentinized ultramafic clasts were analysed for major and selected trace elements by Inductively Coupled Plasma Optical Emission Spectrometry (Thermo ICP-OES Icap 6500) at the SARM (Service d'Analyses des Roches et des Minéraux Nancy, France – Appendix F). This sample set includes 5 Blue-serpentinites recovered at Yinazao (Site U1492, samples: M2, M3, M5, M6, M7), 1 Blue-serpentinite (Site U1496, sample: M24), 4 Liz-serpentinites (Site U1493, samples: TSB55, M9, M10; Site U1496, sample: M19), 2 Atg/Liz-serpentinites (Site U1495, samples: M12, M13), 4 Atg-serpentinites (Site U1495, samples: M14, M15, M16, M17) and 1 Brucitite (Site

U1496, sample: M20) recovered at Asùt Tesoru, 2 Blue-serpentinites (Site U1497, sample: M30; Site U1498, sample: M38), 2 Atg/Liz-serpentinites (Site U1497, sample: M32; Site U1498, sample: M45) and 3 Atg-serpentinites (Site U1497, samples: M50, M51, TSB102) recovered at Fantangisña. Sample digestions for major (SiO_2, Al_2O_3, Fe_2O_3, MnO, MgO, CaO, Na_2O, K2O, TiO_2) and trace elements (Co, Cr, Ga, Ge, Ni, Sc, V, Zn, Cu) were performed on $LiBO_2$ fluxed fusions following the procedures described by Carignan et al. (2001). Boron concentrations were measured by spectrophotometric determination at the SARM. Samples were dissolved by fusion with anhydrous sodium carbonate. The reproducibility of the standard was better than 2% for major elements, 5% for Co, Cr, Ga, Ge, Ni, Sc, V, Zn, B and Li, and 10% for Cu based on repeated analyses of UB-N (serpentinite standard from the Centre de Recherches Pétrographiques et Géochimiques (CRPG) of Nancy, France). The analyses were accurate within 1-5% for SiO_2, Al_2O_3, Fe_2O_3, MnO, MgO, CaO, Na_2O, K_2O and within 1-10% for TiO_2 based on repeated analyses of U.S. Geological Survey, CRPG and Geological Survey of Japan standards BIR-1, UB-N and JP-1, and within 1-10% for Co, Cr, Ga, Ge, Ni, Sc, Cu, Zn, B, Li and better than 15% for V based on UB-N analyses (see Appendix F for comparison with standard preferred values).

A subset of 20 serpentinites was analysed for rare earth elements (REE), Y, Sr, Li, Rb, Cs, Cd, Pb, As, Sb, Ba, U, Th, Nb, Ta, Hf, Zr, V, Ga, Cu and Zn using a High Resolution Sector Field ICP-MS (Element XR) at the Vrije Universiteit Brussel (VUB, Belgium - Appendix F). This sample subset includes 4 Blue-serpentinites recovered at Yinazao (site U1492, samples: M2, M3, M6, M7), 1 Blue-serpentinite (site U1496, sample: M24), 3 Liz-serpentinites (site U1493, samples: TSB55, M9, M10), 2 Atg/Liz-serpentinites (site U1495, samples: M12, M13), 4 Atg-serpentinites (site U1495, samples: M14, M15, M16, M17) and 1 Brucitite (site U1496, sample: M20) recovered at Asùt Tesoru, 2 Blue-serpentinites (site U1497, sample: M30; U1498, sample: M38) and 2 Atg/Liz-serpentinites (site U1497, sample: M32; site U1498, sample: M45) recovered at Fantangisña. Samples were digested with a 1:1 mixture of HCl and HF for 4 days in par bombs. The samples were analysed in low resolution mode after dilution in 2% HNO_3 of 500 for most of trace elements and in medium resolution mode after dilution in 2% HNO_3 of 2000 for Cu, Zn, As, Ba and Pb. The external precision

and accuracy were determined by analysing known ultramafic rock standards (UB-N from the CRPG Nancy, JP-1 from Geological Survey of Japan, PCC-1 and DTS-2b from US Geology Survey). One of the challenges of measuring refractory peridotites is their very low abundance of many trace elements (e.g., REE, HFSE, U, Th, Pb, As). As a consequence, there is a lack of precise and accurate data for reference materials of refractory peridotites (PCC-1, JP-1 and DTS-2b). On the basis of UB-N analysis, reproducibility is better than 10% for most of the trace elements and between 10 and 15% for Hf and Th (see Appendix F). The values obtained for rock standards UB-N, PCC-1, JP-1 and DTS-2b during this study are reported in Appendix F and are in good agreement with previously published data within a 2 standard deviation error.

5. Results and discussion of bulk rock oxygen isotope geochemistry

Results of whole rock analyses are given in Appendix F and are in good agreement with previous studies of serpentinite clasts from nearby seamounts (South Chamorro and Conical; e.g., Kodolanyi et al., 2011; Parkinson & Pearce, 1998; Savov et al., 2005, 2007; Fig. 9) and with the shipboard analyses (Fryer et al., 2018). Relatively low Al_2O_3/SiO_2 (<0.03) and high MgO/SiO_2 (>0.98) of the ultramafic clasts are consistent with a refractory protolith, i.e., dunite or pyroxene-poor harzburgite (e.g., Godard et al., 2008). The high loss on ignition values (>15 wt%) and low SiO_2 contents (<36 wt%) of some samples are in agreement with the crystallization of high amounts of sulfides (e.g. blue serpentinites) and/or brucite during peridotite serpentinization.

Chondrite-normalized REE plots are presented in Fig. 8a. Overall, the studied serpentinites are depleted in REE concentrations compared to chondrite values, and LREE (Light REE, 0.002 to 0.143 chondritic values) are more depleted than HREE (Heavy REE, 0.03 to 0.3 times chondritic values). Among the recovered clasts, two different patterns are observed. Group 1 corresponds to most of the blue serpentinite samples. They are characterized by relatively flat REE patterns with slightly higher concentrations of HREE compared to LREE (La_N/Yb_N = 0.3-0.6; Gd_N/Yb_N = 0.2-0.5; N: Chondrite normalized). This group reflects the pattern of the serpentinite mud erupted at the mud volcanoes (e.g., Savov et al., 2004; Fig. 10a) and may therefore reflect late stage re-equilibration between the mud and the ultramafic clasts.

Group 2 includes blue-, Liz-, Atg/Liz- and Atg- serpentinites. These samples display U-shape REE patterns, with depletion in the MREE (Middle Rare Earth Elements) relative to the LREE (La_N/Yb_N = 0.03-2) and HREE (Gd_N/Yb_N = 0.02-0.4; Fig. 10a), and also possess positive Eu anomalies (Eu/Eu* = $Eu_N/[(Sm_N+Gd_N)/2]$). The LREE concentrations progressively increase from the Liz-serpentinites (La_N/Yb_N = 0.04-0.13) to the Atg/Liz- (La_N/Yb_N = 0.12-2) and Atg-serpentinites (La_N/Yb_N =0.1-0.4). The Eu anomaly is more pronounced in Liz- and Atg/Liz-serpentinites (Eu/Eu* = 0.9-6.8) relative to Atg-serpentinites (Eu/Eu* = 0.7-1.8). These patterns are similar to those reported in the Conical mud volcano and have been interpreted as inherited from the peridotite protolith (Parkinson and Pearce, 1998). In Fig. 10b, Group 2 serpentinites are characterized by a strong depletion in most incompatible elements with respect to primitive mantle. The studied clasts show enrichments in Cs (Cs_n/La_n > 21; n: Primitive Mantle normalization) and positive anomalies in U (U_n/Th_n > 2), Pb (Pb_n/La_n > 4), Sr (Sr_n/Pr_n > 2), As, Sb (As_n/Pr_n > 1500) and Li (Li* > 60, Li* = Li / [Dy/2 + Y/2]).

Variations of fluid mobile elements (FME) and metal concentrations are observed for the different serpentinite types. The concentrations of As and Sb are lower in Liz-serpentinites (As = 0.7-1.3 ppm; Sb <0.001 ppm;) compared to Atg-serpentinites (As = 1.5-9.2 ppm; Sb = 0.03-0.21 ppm; B = 10-97 ppm), whereas Li (from 4-6 ppm to 0.4-0.8 ppm), Sr (from 1-8.5 ppm to 0.1-1 ppm) and Cs (from 0.14-0.22 ppm to <0.01-0.03 ppm) concentrations decrease from Liz- to Atg- serpentintes (Fig. 11). B and Zn concentrations are relatively constant in Liz- (B = 20-30 ppm; Zn = 35-65 ppm), Atg/Liz- (B = 48-59 ppm, Zn = 48-55 ppm) and Atg-serpentinites (B = 10-49 ppm; Zn = 36-52 ppm). It should be noted that boron (B) is highly enriched on all the studied samples relative to primitive mantle (B_{PM} = 0.19 ± 0.02 ppm, PM: Primitive Mantle; Marschall et al., 2017). Of all samples, blue serpentinites are characterized by the highest Zn (51-92 ppm), and highly variable Sr (2-28 ppm) and B (7-250 ppm) concentrations (Fig. 11c; Appendix F). It is unknown whether or not these elements are solely carried by serpentine minerals, which can incorporate these elements in its structure (e.g., Pabst et al., 2011; Debret et al., 2017), or by other accessory (micro- to nano-) phases (e.g., sulfides, spinels, hydro-garnets…).

Eight serpentine separates have $\delta^{18}O_{Srp}$ values of 5.8 to 8.3‰ (Table 1), overlapping with the range of analyses from previous Mariana mud volcano studies (6.5 to 10.8‰, reported by Alt & Shanks, 2006; 5.8 to 8.5‰ by Sakai et al., 1990; 6.1 to 10.5‰ by Kahl et al., 2015), and one magnetite separate has $\delta^{18}O_{Mgt}$ value of 1.8‰ (Table 1), in good agreement with Alt and Shanks (2006) who reported $\delta^{18}O_{Mgt}$ values of 0 to 2‰ in antigorite-rich samples. No obvious changes of $\delta^{18}O_{Srp}$ are observed with increasing distance from the trench in this study ($\delta^{18}O_{srp}$ [Yinazao] = 6.4 ‰; $\delta^{18}O_{Srp}$ [Fantangisña] = 8.3 ‰; $\delta^{18}O_{srp}$ [Asùt Tesoru] = 5.8-8.3 ‰) or in previous studies ($\delta^{18}O_{srp}$ [S. Chamorro] = 6.4-10.5 ‰; $\delta^{18}O_{srp}$ [Conical] = 6.1-10.8 ‰; Alt and Shanks, 2006; Kahl et al., 2015; Sakai et al., 1990). However, systematic variations of $\delta^{18}O_{Srp}$ relative to sample mineralogy and in pore fluids are observed. Blue serpentine displays $\delta^{18}O$ values ranging from 6.4 to 7.4‰, whereas higher $\delta^{18}O$ values are observed in Liz-serpentinites ($\delta^{18}O_{serp}$ 6.8 to 7.6‰) compared to Atg/Liz-serpentinites ($\delta^{18}O_{srp.}$ 5.8 to 6.1‰). Antigorite in the Atg-serpentinites records $\delta^{18}O_{Srp}$ values varying from 7.1 to 8.3‰, whereas associated magnetite has a $\delta^{18}O_{Mgt}$ value of 1.8 ‰. Pore fluid $\delta^{18}O$ values range from -1.39 to -0.14‰ in Yinazao, from -0.03 to 0.25‰ in Fantangisña and from 1.73 to 1.97‰ in Asùt Tesoru. Although highly variable with depth, these values suggest an increase in the $\delta^{18}O$ values of the pore fluid from shallow Yinazao (mean $\delta^{18}O_{fluid}$ = -0.90‰, n = 10) to the deeper Fantangisña (mean $\delta^{18}O_{fluid}$ = 0.11‰, n = 6) or Asùt Tesoru (mean $\delta^{18}O_{fluid}$ = 1.83‰, n = 4; Fig. 12). These values are significantly lower than those reported for South Chamorro (mean $\delta^{18}O_{fluid}$ = 2.5‰) and Conical (mean $\delta^{18}O_{fluid}$ = 4‰; Mottl et al., 2003), which are further from the trench.

6. Reconstructing forearc serpentinization conditions

Textural relationships between the different serpentine generations allow the reconstruction of a semi-quantitative temperature evolution of the serpentinization conditions within the Marianas forearc mantle wedge and thus a discussion of subduction dynamics. Forearc mantle wedge peridotites are former sub-arc peridotites that underwent extensive partial melting before being dragged into the forearc by mantle convection (e.g. Parkinson & Pearce, 1998). These peridotites are hydrated by slab-derived fluids and progressively transformed into serpentinites. The formation of early brown lizardite bearing veins crosscutting olivine and orthopyroxene in Liz-serpentinites (Fig. 6a) constitutes the first stage of the forearc mantle wedge hydration and serpentinization. These textures have been observed

at the Fantangisña and Asùt Tesoru mud volcanoes as well as at the South Chamorro and Conical mud volcanoes during previous IODP expeditions (e.g. Kahl et al., 2015). The presence of significant amounts of brucite in Liz-serpentinites (Figs 5, 6a) can be attributed to the refractory composition of forearc mantle peridotites. In Mg-rich systems and at low-temperatures (e.g., Klein et al., 2014), the serpentinization of olivine results in magnesium excess allowing brucite precipitation:

(1) $2\ Fe_{0.15}Mg_{1.85}SiO_4 + 3\ H_2O = Fe_{0.2}Mg_{0.8}OH_2 + Fe_{0.1}Mg_{2.9}Si_2O_5(OH)_4$

Olivine + Water = Fe-brucite + Lizardite

Here the XMg of brucite is assumed to be 0.8 based on linear regression of microprobe analyses (Fig. 5). Although lizardite and brucite can coexist over a large range of temperatures during the serpentinization process, the absence of magnetite during brown serpentine crystallization suggests rather low serpentinization temperature (< 200°C; Bonnemains et al., 2016; Klein et al., 2014). Assuming equilibria between lizardite and associated pore fluids, serpentine crystallisation temperatures (Table 1) were calculated based on the serpentine–water oxygen isotope fractionation from Saccocia et al. (2009). In agreement with petrographic observation, the temperature estimates of lizardite crystallization vary between 203 and 211°C (Table 1). It should, however, be noted that we cannot exclude an intergrowth of the serpentine separates with microscale brucite; such impurities would then lead to an overestimation of the calculated temperatures, as discussed by Alt and Shanks (2006). The crystallization temperatures estimates must therefore be considered as maxima.

The crystallization of antigorite at the expense of lizardite-bearing textures has been observed at Fantangisña and Asùt Tesoru in Atg/Liz-serpentinites and has also been reported at South Chamorro and Conical mud volcanoes (e.g. Alt and Shanks, 2006). The formation of antigorite corresponds to a second stage of serpentinization that is accompanied with the precipitation of large amounts of magnetite and the crystallization of Mg-rich brucite (XMg ~ 0.9; Figs 7 and 8). The transition of lizardite to antigorite in subduction settings is commonly interpreted to result from increasing P-T conditions during prograde metamorphism (Debret et al., 2013; Evans, 2004; Scambelluri et al., 2004; Schwartz et al., 2013; Wunder et al., 2001). The $\delta^{18}O$ values of serpentine minerals crystallizing in

Atg/Liz-serpentinites indicate crystallisation temperatures of 230-240°C if we assume equilibria between serpentine and associated pore fluids. Those estimates are however at the lower range of previous thermodynamic estimates or natural observations that predict the coexistence of lizardite and antigorite during subduction between about 250-350°C (Evans, 2004; Schwartz et al., 2013). Indeed, based on combined δD and $\delta^{18}O$ values of serpentine from Conical ultramafic clasts, Alt and Shanks (2006) propose that the serpentinizing fluids released by the subducting slab at depth are likely to increase with temperature and to be progressively enriched in ^{18}O ($\delta^{18}O_{fluid}$ ~ 5.5‰ at 250°C and ~ 9.0‰ at 400°C; Fig. 12). Similarly, Sakai et al. (1990) also suggest a slab-derived fluid with a $\delta^{18}O$ value of approximately 3.0‰ based on the oxygen and hydrogen isotope composition of Izu and Mariana forearc serpentinite clasts. In agreement with those studies, we observed a progressive increase of $\delta^{18}O$ values of pore fluids with increasing distance from the trench (Fig. 12). However, pore fluid measurements from Yinazao, Fantangisña or Asùt Tesoru (-1.39 to +1.97 ‰) are always lower than $\delta^{18}O$ estimates of slab-derived fluids suggesting that the $\delta^{18}O$ values of pore fluids are driven toward to lower values during serpentinization processes occurring within the forearc (Alt and Shanks, 2006). In agreement with this scenario, the $\delta^{18}O_{Srp}$ analyses are more or less constant and enriched in ^{18}O (5.8-10.8 ‰; e.g., Alt and Shanks, 2006; Kahl et al., 2015; Sakai et al., 1990; this study) relative to pore fluids analyses, regardless of the slab depth. Higher $\delta^{18}O$ values for pore fluids than those recorded here have been reported by Mottl et al. (2003) for the more distant South Chamorro ($\delta^{18}O_{fluid}$ = 2.5 ± 0.5 ‰) and Conical ($\delta^{18}O_{fluid}$ = 4 ± 0.5 ‰) mud volcanoes (Fig. 12). If these higher pore fluid $\delta^{18}O$ values are used, temperature estimates are somewhat higher at 243-283°C for serpentine crystallization in Atg/Liz-serpentinites and therefore in better agreement with previous estimates of the transition lizardite to antigorite in subduction zones (250-350°C; Schwartz et al., 2013).

The observation of euhedral magnetite embedded in brucite in Atg-serpentinites (Figs 6b, 7b and 8b) suggests equilibrium with brucite, which in turn formed in equilibrium with antigorite. We therefore use the $\delta^{18}O$ values of serpentine–magnetite pairs to estimates the temperature of antigorite crystallization (thermometer of Wenner & Taylor, 1971 revised by Früh-Green et al., 1996) as 322 to

409°C. These temperatures overlap or are slightly higher compared to previous estimates of 300–375°C from Alt & Shanks (2006), and suggest that the transition of lizardite to antigorite in the forearc mantle likely occurs in a temperature range of 200 to 320°C. These estimates are also in accordance with thermodynamic calculations by Evans (2004) predicting the assemblage antigorite + brucite to be more stable than lizardite and chrysotile at temperatures > 300°C.

The transition from lizardite to antigorite can follow different reactions (e.g., Evans, 2004; Vils et al., 2011). For example, in a water saturated open system, the transition can be written in a MASH system as (Evans, 2004):

(2) $16\ Mg_3Si_2O_5(OH)_4 + 2\ SiO_{2(aq)} = 16\ Mg_3Si_{2.125}O_{5.31}(OH)_{3.875} + H_2O_{(aq)}$

$$\text{Lizardite} + SiO_{2(aq)} \rightarrow \text{antigorite} + H_2O_{(aq)}$$

whereby the required influx of SiO_2 could be generated by sediment dehydration (e.g. Deschamps et al., 2011; Schwartz et al., 2013). However, the absence of a SiO_2-rich phase (e.g. talc, diopside) and the high amounts of brucite (Figs 7 and 8) rather suggest a system with low SiO_2 activity. The high amounts of brucite formed during mantle wedge serpentinization are also in line with former studies of the Mariana forearc (e.g., D'Antonio & Kristensen, 2004; Murata et al., 2009) and mantle wedge relicts from the Sanbagawa Belt (southwest Japan, Kawahara et al., 2016). These observations suggest a limited transfer of SiO_2 during slab dehydration at shallow depth.

In our samples, the antigorite-forming alteration stage is accompanied by a decrease of FeO in serpentine and brucite minerals suggesting a redistribution of Fe between Fe-bearing minerals. In order to account for the production of brucite and magnetite during the recrystallization of lizardite into antigorite without the addition of SiO_2 by fluids, we propose the following equation:

(3) $Fe_{0.2}Mg_{0.8}OH_2 + Fe_{0.1}Mg_{2.9}Si_2O_5(OH)_4 = Fe_{0.08}Mg_{0.92}(OH)_2 + Fe_{0.04}Mg_{2.78}Si_2O_5(OH)_{3.64} + 0.04\ Fe_3O_4 + 0.24\ H_2O + 0.06\ H_2$

$$\text{Fe-Brucite} + \text{Fe-Lizardite} = \text{Brucite} + \text{Antigorite} + \text{Magnetite} + H_2O + H_2$$

521 with the XMg of antigorite and brucite derived from microprobe analyses. It should be noted that this
522 equation does not take into account the potential incorporation of Fe^{3+} into serpentine minerals
523 (Andreani et al., 2013; Debret et al., 2014), the potential mobility of Fe in slab derived fluids (Debret
524 et al., 2016), nor the role of other redox sensitive elements (e.g., C or S). Hence the production of H_2
525 in the equation is speculative.

526 The studied samples were partly affected by late serpentinization stages characterised by the
527 crystallization of blue serpentine and sulfides (Fig. 3). If present, this late serpentinization stage
528 largely replaces former textures, i.e. serpentine or mantle minerals (see Appendix A). This alteration
529 texture is highly developed in Yinazao, whereas it is limited to the uppermost units of Fantangisña and
530 Asùt Tesoru mud volcanoes suggesting that the crystallization of blue serpentine mainly occurs as a
531 late stage of serpentinization. Large amounts of sulfides in some of these samples may indicate
532 ongoing reduction of sulfates to sulfides through the activity of microbial communities (e.g., Mottl et
533 al., 2003) during this stage. These sulfides display framboidal textures that are commonly interpreted
534 as microbe-derived textures formed during bacterially mediated sulfate reduction (e.g., Thiel et al.,
535 1999; Wilkin and Barnes, 1997). However, based on $\delta^{18}O$ analyses, the temperature estimates of blue
536 serpentine crystallization vary between 183 and 194°C (Table 1), higher than those considered
537 feasible for life (~ 122°C; Kashefi and Lovley, 2003). It should be noted that these temperature
538 estimates are maxima due to brucite/serpentine intergrowths in serpentine textures in the blue-
539 serpentinites, as discussed above. It is thus possible that the blue serpentinites formed at temperatures
540 lower than 122°C. In addition, recent investigations of Mariana ultramafic clasts show the possible
541 existence of microbial ecosystems within or below the Mariana mud volcanoes (Plümper et al., 2017).
542 Microbial activity may therefore have taken place at a similar time to the crystallization of blue-
543 serpentine in these sub-surface environments.

544 The temperatures of the slab / forearc mantle interface have previously been estimated to be ~80°C
545 below Yinazao and to be ~250°C below Asùt Tesoru (Hulme et al., 2010), in both cases using pore
546 water chemistry. These estimates are significantly lower than ours derived from oxygen isotope
547 thermometry (up to about 400°C) and incompatible with antigorite crystallization in a subduction

548 setting (Evans, 2004; Schwartz et al., 2013). Although recent studies have reported the crystallization
549 of antigorite in an oceanic setting at relatively low temperatures (e.g., Rouméjon et al., 2014), this has
550 been attributed to Si-metasomatism, possibly following pyroxene serpentinization, and is not
551 compatible with SiO_2 undersaturated systems. The occurrence of antigorite in our samples rather
552 suggests a progressive increase in temperature leading to the formation of antigorite, magnetite and
553 Fe-poor brucite at the expense of lizardite. This scenario is compatible with a progressive burial of the
554 forearc mantle wedge during subduction.

555 The deep burial of forearc rocks can be due to either corner flow enhanced by the low viscosity of
556 serpentinite (e.g. Nagaya et al., 2016) or to frictional stresses mechanically disaggregating the slab
557 surface and eroding the mantle wedge above the décollement zone, incorporating serpentinized mantle
558 into the aggregated subducting inventory (e.g., King et al., 2006). Both processes could potentially
559 explain a prograde metamorphic path and the coexistence of ultramafic clasts displaying various
560 mineralogical assemblages equilibrated at various temperatures in each of the mud volcanoes. The
561 ultimate mechanism responsible for carrying the clasts to depth remains unclear and requires a detailed
562 textural investigation, which is beyond the scope of this study. However, retrograde processes leading
563 to the overprinting of high-temperature serpentine phases by lower-temperature chrysotile (± lizardite)
564 such as those observed here are interpreted to occur during the rise of the clasts towards shallower
565 levels in the forearc, e.g., in the mud volcano conduits. The recovered clasts display a high degree of
566 serpentinization (most of the clasts are serpentinized to almost 100%) compared to geophysical data
567 based on seismic velocities which suggest serpentinization $\geq$ 30 % in the forearc (Reynard, 2013).
568 These conflicting observations can be reconciled if only low density material (i.e., highly
569 serpentinized parts of the forearc) can be exhumed, probably by buoyancy (e.g. Guillot et al., 2000),
570 during subduction.

571 Similar observations of prograde and retrograde metamorphism in the Mariana forearc peridotites
572 were described by Murata et al. (2009), who recognized lower-temperature chrysotile veins in
573 antigorite-rich clasts that both pre- and post-date high-temperature antigorite growth. The authors
574 concluded that this reflected a complex process of tectonic cycling of shallow mantle wedge

peridotites to depth and then back again to the surface. Several other studies have also noted the possibility that serpentinite formed in the shallower parts of the subduction zone may be carried deeper into the subduction zone (e.g., Kawahara et al., 2016; Kerrick & Connolly, 2001; Savov et al., 2005, 2007; Snyder et al., 2005; Tamblyn et al., 2018). This suggests that the serpentinized forearc mantle wedge can significantly contribute to arc magmas isotope and elemental budget during subduction (e.g., Ribeiro and Lee, 2017; Debret et al., 2018a).

7. Evolution of forearc mantle wedge composition during subduction

Mariana forearc mud volcanoes are formed by the interaction of slab-derived fluids and forearc peridotites. The nature of the fluids released during slab dehydration is expect to change considerably with increasing depth and associated increase of pressure and temperature at depth (Bebout, 2013 and reference therein). Previous analyses of pore water chemistry of Mariana ultramafic clasts have shown an increase in K, sulfate, carbonate alkalinity, Na/Cl, B, Mn, Fe, Co, Rb, Cs, Gd/Tb, Eu, and LREE and a decrease in Ca, Sr, and Y with depth to the slab/mantle interface (Fryer et al., 2018; Hulme et al., 2010; Mottl et al., 2003). In agreement with these observations, we observed an increase of $\delta^{18}O$ values of pore fluids from Yinazao to Asùt Tesoru and the deeper-sources South Chamorro and Conical mud volcanoes (Fig. 12). However, the bulk-rock major and trace element compositions of serpentinized clasts recovered from Yinazao, Fantangisña, Asùt Tesoru, South Chamorro and Conical mud volcanoes largely overlap and therefore do not reflect these strong variations (Fig. 9 and 11). This is in good agreement with petrographic observations showing the existence of up and down movements beneath serpentinite mud volcanoes (e.g. Kawahara et al., 2016 or this study). We do however observe modifications of clasts chemistry according to mineralogy, i.e., Blue-, Liz-, Atg/Liz- and Atg- serpentinites.

The first step of serpentinization of the forearc mantle corresponds to the formation of brown serpentine (Liz-serpentinite), a mixture of chrysotile/lizardite with Fe-rich brucite, at the expense of mantle minerals (Fig. 13). As previously documented (e.g., Kahl et al., 2015; Peters et al., 2017; Savov et al., 2005, 2007), lizardite-dominated samples are characterized by high concentrations of fluid mobile elements (FME), such as B, Li, Cs, As, Sb, relative to primitive mantle and/or abyssal

serpentinite/peridotite (Fig. 11). These enrichments have been attributed to the influx of slab-derived fluids in the forearc mantle at intermediate temperatures (200-500°C). The onset of subduction is accompanied by large amounts of compaction, deformation and metamorphic reactions (e.g. clay mineral or carbonate breakdown) in the slab resulting in the release of FME-rich fluids (e.g., Barnes et al., 2014; Bebout, 2013; Cannaò et al., 2015; Debret et al., 2013, 2018a; Hattori & Guillot, 2007). The transfer of such fluids to the overlying fore-arc mantle wedge allows its serpentinization and the storage of FME in forearc serpentinites.

The progressive burial of ultramafic material is accompanied by the recrystallization of Liz-serpentinites to antigorite, i.e., Atg/Liz- and Atg-serpentinites (Fig. 13). During this transformation, Cs, Li and Sr concentrations in serpentinites progressively decrease. Indeed, although a relatively small amount of water is released during the transition of lizardite to antigorite (e.g. Evans, 2004), this reaction can be accompanied with dissolution and leaching of C- and/or S- bearing phases (e.g. Debret et al., 2014) and FME released in fluids (e.g., Debret et al., 2013; Kodolányi & Pettke, 2011; Vils et al., 2011) suggesting that these elements are highly mobile in fluids during forearc burial. Boron concentrations remain high in Atg/Liz- and Atg-serpentinites relative to slab serpentinites (e.g., Vils et al., 2011; Debret et al., 2013) and/or abyssal peridotites/serpentinites (Andreani et al., 2009). This suggests that antigorite also crystallizes in equilibrium with B-rich slab derived fluids. *In situ* analyses of partly serpentinized forearc peridotites reveal that, in low temperature lizardite bearing serpentinites (< 200°C), serpentine textures integrate high amounts of B (up to 200 ppm, Pabst et al, 2011; Kahl et al., 2014). These values are close to those reported in antigorite bearing textures in mantle wedge settings (e.g., Deschamps et al., 2010). Hence, the absence of correlation between B concentrations and indices of prograde metamorphism suggests that, during the serpentinization of the forearc, saturation (or exchange equilibrium – e.g., Pabst et al., 2011) is rapidly reached in the serpentine, i.e., before the transition from lizardite to antigorite. In agreement with these observations, sediment pore water chemistry reveals progressive enrichments in Cs, Li and B concentrations with increasing distance to the trench (Fryer et al., 2018; Hulme et al., 2010; Mottl et al., 2003) confirming that these elements become progressively abundant in fluids during the progressive burial of the forearc (e.g., De

629 Hoog and Savov, 2018). In contrast to other fluid mobile elements, the concentrations of As, Sb and
630 LREE progressively increase in whole rocks during the transition of lizardite to antigorite (Figs 9 and
631 10). Previous studies have shown that these elements can be incorporated in antigorite (e.g., Hattori et
632 al., 2005). Fluids released during the early (shallow) stage of slab devolatilization are likely dominated
633 by diagenesis and opal dehydration, whereas later (deeper) processes included decarbonation and clay
634 mineral decomposition resulting in a modification of slab derived fluid composition (Bebout, 2013 and
635 reference therein). As, Sb and the LREE are enriched in fluids derived from sediment decarbonation
636 (Bebout, 2013; Debret et al., 2018a). Hence, we interpret the high As, Sb and LREE concentrations of
637 the antigorite dominated serpentinites in terms of the onset of carbonate dissolution within the slab
638 (e.g., carbonated altered oceanic crust). This scenario is in good agreement with high dissolved
639 inorganic carbon concentrations of pore fluids from the furthest mud volcanoes (Asùt Tesoru, South
640 Chamorro and Conical; Fryer et al., 2018).

641 During their exhumation forearc serpentinites are partly to fully recrystallized into blue serpentine.
642 This episode is accompanied with a flattening of REE patterns (Fig. 10a – Group 1), probably linked
643 to a high mobility of LREE in fluids (e.g., Fryer et al., 2018), and an increase in Zn concentrations
644 (Fig. 11c). This observation suggests that the composition serpentinites recorded at depth can be partly
645 overprinted by low-temperature reactions (< 250°C) during clast exhumation. However, the exact
646 source of the added Zn is unclear as Zn can be mobile in fluids either at depth during serpentinite
647 devolatilization (Pons et al., 2016), decarbonation processes (Debret et al., 2018a; Inglis et al., 2017)
648 as well as near the seafloor through hydrothermal fluid circulation Debret et al., 2018b) and microbial
649 activity via sulfate reduction (Kelley et al., 2009).

650 **8. Conclusions**

651 Our study reveals that the ultramafic clasts recovered in serpentinite mud volcanoes record three main
652 stages of serpentinization (Fig. 13): the crystallization of brown serpentine bearing textures composed
653 of a mixture of Fe-rich brucite and chrysotile and/or lizardite (stage 1 in Fig. 13); the formation of
654 antigorite in equilibrium with magnetite and Fe-poor brucite at the expense of brown serpentine
655 (stages 2 to 3 in Fig. 13); the late formation of blue serpentine associated with frambroidal sulfides

during the exhumation of the ultramafic clasts (stage 4 in Fig. 13). The transition of lizardite to antigorite is enhanced by an increase of temperature from 200°C up to about 400°C within the forearc area. These estimates are in good agreement with thermodynamic calculations carried out by Evans (2004). The crystallization of antigorite at the expense of lizardite has been observed in different mud-volcanoes. Although most of the blue serpentine was observed at Yinazao, there is no evidence for a systematic serpentine phase change according to depth of the slab/mantle interface. These observations suggest the existence of complex transport mechanisms below the mud volcanoes, with the serpentinites being progressively dragged down to greater depth before their exhumation, potentially controlled by buoyancy, toward to the surface. In agreement with this scenario, no obvious changes of serpentinite clasts chemistry is observed according to depth to the slab/mantle interface (Fig. 9-11).In contrast, the crystallization of lizardite and then antigorite in serpentinites is accompanied with a decrease of Cs, Li, Sr and an increase in As, Sb and LREE concentrations in whole rock, whereas B concentrations are relatively constant. This suggests that the serpentinized mantle wedge acts as a filter for trace elements and controls the fluxes of these elements between the surface and the deep mantle. The fluid release during shallow metamorphic reactions (i.e., transition lizardite to antigorite) are likely to feed hydrothermal circulation near the surface. In contrast, the dragged down residue (Atg-serpentinites) will undergo a progressive increase in temperature, coupled to the ongoing burial, until its dehydration at greater depth. This process will release large amounts of fluid, thereby contributing to arc magmas genesis in subduction zones.

Acknowledgements

We are grateful to the crew of the D/V JOIDES Resolution and to the science party of IODP Expedition 366, especially to P. Fryer, G. Wheat, T. Williams, V. Magalhaes, K. Johnson, R.M. Johnson, W. Kurz, K. Michibayashi, J.W. Park, J.G. Ryan, J.W. Shervais and S.S. Mantovanelli for constructive discussions. We also thank J.-L. Devidal (Magmas et Volcans, Clermont-Ferrand) for his help during microprobe analyses, Y. Géraud (Georessources, Nancy) for his help during major elements analyses at the SARM and S. Goderis (VUB, Brussels) for his assistance during trace element analyses. M. Cisneros is thanked for help with stable isotope analyses. This work was fund by

683 a NERC Moratorium Award (n°XXXXX) and by the F.N.R.S. BD acknowledges his F.R.S.-F.N.R.S.
684 research fellowship (Chargé de recherche). EA acknowledges funding by the German Research
685 Foundation, Special Priority Program 527 (IODP/ODP; grant BA 1605/18-1). BW acknowledges
686 funding by IODP-France. REP acknowledges funding from the U.S. Science Support Program
687 (USSSP) post-expedition activity (PEA) We thank I. Savov and an anonymous reviewer for critical
688 comments on earlier version of this article and careful editorial handling by M. Scambelluri.

689

690 **References**

691 Alt, J.C., Shanks, W.C., 2006. Stable isotope compositions of serpentinite seamounts in the Mariana
692 forearc: Serpentinization processes, fluid sources and sulfur metasomatism. Earth Planet. Sci.
693 Lett. 242, 272–285. https://doi.org/10.1016/j.epsl.2005.11.063

694 Andreani, M., Muñoz, M., Marcaillou, C., Delacour, A., 2013. μXANES study of iron redox state in
695 serpentine during oceanic serpentinization. Lithos 178, 70–83.
696 https://doi.org/10.1016/j.lithos.2013.04.008

697 Augustin, N., Lackschewitz, K.S., Kuhn, T., Devey, C.W., 2008. Mineralogical and chemical mass
698 changes in mafic and ultramafic rocks from the Logatchev hydrothermal field (MAR 15°N).
699 Mar. Geol. 256, 18–29. https://doi.org/10.1016/j.margeo.2008.09.004

700 Barnes, J.D., Beltrando, M., Lee, C.T.A., Cisneros, M., Loewy, S., Chin, E., 2014. Geochemistry of
701 Alpine serpentinites from rifting to subduction: A view across paleogeographic domains and
702 metamorphic grade. Chem. Geol. 389, 29–47. https://doi.org/10.1016/j.chemgeo.2014.09.012

703 Beard, J.S., Frost, B.R., Fryer, P., McCaig, a., Searle, R., Ildefonse, B., Zinin, P., Sharma, S.K., 2009.
704 Onset and Progression of Serpentinization and Magnetite Formation in Olivine-rich Troctolite
705 from IODP Hole U1309D. J. Petrol. 50, 387–403. https://doi.org/10.1093/petrology/egp004

706 Bebout, G.E., 2013. Chemical and Isotopic Cycling in Subduction Zones, in: Treatise on
707 Geochemistry: Second Edition. pp. 703–747. https://doi.org/10.1016/B978-0-08-095975-
708 7.00322-3

709 Bonnemains, D., Carlut, J., Escarti-n, J., Mével, C., Andreani, M., Debret, B., 2016. Magnetic
710 signatures of serpentinization at ophiolite complexes. Geochemistry, Geophys. Geosystems 17,
711 2969–2986. https://doi.org/10.1002/2016GC006321

712 Boschi, C., Bonatti, E., Ligi, M., Brunelli, D., Cipriani, A., Dallai, L., D'Orazio, M., Früh-Green,
713 G.L., Tonarini, S., Barnes, J.D., Bedini, R.M., 2013. Serpentinization of mantle peridotites along
714 an uplifted lithospheric section, mid atlantic ridge at 11° N. Lithos 178, 3–23.

https://doi.org/10.1016/j.lithos.2013.06.003

Bostock, M.G., Hyndman, R.D., Rondenay, S., Peacock, S.M., 2002. An inverted continental moho and serpentinization of the forearc mantle. Nature 417, 536–538. https://doi.org/10.1038/417536a

Cannaò, E., Agostini, S., Scambelluri, M., Tonarini, S., Godard, M., 2015. B, Sr and Pb isotope geochemistry of high-pressure Alpine metaperidotites monitors fluid-mediated element recycling during serpentinite dehydration in subduction mélange (Cima di Gagnone, Swiss Central Alps). Geochim. Cosmochim. Acta 163, 80–100. https://doi.org/10.1016/j.gca.2015.04.024

Carignan, J., Hild, P., Mevelle, G., Morel, J., Yeghicheyan, D., 2001. Routine Analyses of trace Elements in Geological Samples using Flow injection and Low Pressure On-Line liquid Chromatography Coupled to ICP-MS : A study of Geochemical Reference Materials BR, DR-N, UB-N, AN-G and GH. Geostand. Newsl. 25, 187–198. https://doi.org/10.1111/j.1751-908X.2001.tb00595.x

Chemenda, A.I., Mattauer, M., Malavieille, J., Bokun, A.N., 1995. A mechanism for syn-collisional rock exhumation and associated normal faulting: result from physical modelling. Earth Planet. Sci. Lett. 132, 225–232.

Christensen, N.I., 2004. Serpentinites, Peridotites, and Seismology. Int. Geol. Rev. 46, 795–816. https://doi.org/10.2747/0020-6814.46.9.795

D'Antonio, M., Kristensen, M.B., 2004. Serpentine and brucite of ultramafic clasts from the South Chamorro Seamount (Ocean Drilling Program Leg 195, Site 1200): inferences for the serpentinization of the Mariana forearc mantle. Mineral. Mag. 68, 887–904. https://doi.org/10.1180/0026461046860229

DeHoog, C.J. and Savov, I. P., 2018. Boron Isotopes as a Tracer of Subduction Zone Processes. In: Marschall H., Foster G. (eds) Boron Isotopes. Advances in Isotope Geochemistry. Springer Cham, 217-247, DOI: 10.1007/978-3-319-64666-4_9

Debret, B., Andreani, M., Godard, M., Nicollet, C., Schwartz, S., Lafay, R., 2013. Trace element

behavior during serpentinization/de-serpentinization of an eclogitized oceanic lithosphere: A LA-ICPMS study of the Lanzo ultramafic massif (Western Alps). Chem. Geol. 357, 117–133. https://doi.org/10.1016/j.chemgeo.2013.08.025

Debret, B., Andreani, M., Muñoz, M., Bolfan-Casanova, N., Carlut, J., Nicollet, C., Schwartz, S., Trcera, N., 2014. Evolution of Fe redox state in serpentine during subduction. Earth Planet. Sci. Lett. 400, 206–218. https://doi.org/10.1016/j.epsl.2014.05.038

Debret, B., Beunon, H., Mattielli, N., Andreani, M., Ribeiro da Costa, I., Escartin, J., 2018b. Ore component mobility, transport and mineralization at mid-oceanic ridges: A stable isotopes (Zn, Cu and Fe) study of the Rainbow massif (Mid-Atlantic Ridge 36◦14_N). Earth Planet. Sci. Lett. 503, 170-180. https://doi.org/10.1016/j.epsl.2018.09.009

Debret, B., Bouilhol, P., Pons, M.L., Williams, H., 2018a. Carbonate transfer during the onset of slab devolatilization: new insights from Fe and Zn stable isotopes. Journal of Petrology 59, 1145-1166.

Debret, B., Millet, M.A., Pons, M.L., Bouilhol, P., Inglis, E., Williams, H., 2016. Isotopic evidence for iron mobility during subduction. Geology 44, 215–218. https://doi.org/10.1130/G37565.1

Debret, B., Nicollet, C., Andreani, M., Schwartz, S., Godard, M., 2013. Three steps of serpentinization in an eclogitized oceanic serpentinization front (Lanzo Massif - Western Alps). J. Metamorph. Geol. 31, 165–186. https://doi.org/10.1111/jmg.12008

Delacour, A., Früh-Green, G.L., Bernasconi, S.M., 2008. Sulfur mineralogy and geochemistry of serpentinites and gabbros of the Atlantis Massif (IODP Site U1309). Geochim. Cosmochim. Acta 72, 5111–5127. https://doi.org/10.1016/j.gca.2008.07.018

Deschamps, F., Guillot, S., Godard, M., Andreani, M., Hattori, K., 2011. Serpentinites act as sponges for fluid-mobile elements in abyssal and subduction zone environments. Terra Nov. 23, 171–178. https://doi.org/10.1111/j.1365-3121.2011.00995.x

Deschamps, F., Guillot, S., Godard, M., Chauvel, C., Andreani, M., Hattori, K., 2010. In situ

765 characterization of serpentinites from forearc mantle wedges: Timing of serpentinization and
766 behavior of fluid-mobile elements in subduction zones. Chem. Geol. 269, 262–277.
767 https://doi.org/10.1016/j.chemgeo.2009.10.002

768 Dubois-Côté, V., Hébert, R., Dupuis, C., Wang, C.S., Li, Y.L., Dostal, J., 2005. Petrological and
769 geochemical evidence for the origin of the Yarlung Zangbo ophiolites, southern Tibet. Chem.
770 Geol. 214, 265–286. https://doi.org/10.1016/j.chemgeo.2004.10.004

771 Evans, B.W., 2004. The Serpentinite Multisystem Revisited : Chrysotile Is Metastable. Int. Geol. Rev.
772 46, 479–506.

773 Faria, D.L.A. De, Vena, S., 1997. Raman Microspectroscopy of Some Iron Oxides and
774 Oxyhydroxides. J. Raman Spectrosc. 28, 873–878.

775 Frost, B.R., 1985. On the stability of sulfides, oxides, and native metals in serpentinite. J. Petrol. 26,
776 31–63. https://doi.org/10.1093/petrology/26.1.31

777 Frost, B.R., Beard, J.S., 2007. On Silica Activity and Serpentinization. J. Petrol. 48, 1351–1368.
778 https://doi.org/10.1093/petrology/egm021

779 Fruh-Green, G.L., Plas, A., Lecuyer, C., 1996. Petrologic and Stable Isotope Constraints on
780 Hydrothermal Alteration and Serpentinization of the EPR Shallow Mantle at Hess Deep (Site
781 895). Proc. Ocean Drill. Program, 147 Sci. Results 147.
782 https://doi.org/10.2973/odp.proc.sr.147.016.1996

783 Fryer, P., 2012. Serpentinite Mud Volcanism: Observations, Processes, and Implications. Ann. Rev.
784 Mar. Sci. 4, 345–373. https://doi.org/10.1146/annurev-marine-120710-100922

785 Fryer, P., 1996. Evolution of the Mariana convergent plate margin system. Rev. Geophys. 34, 89–125.
786 https://doi.org/10.1029/95RG03476

787 Fryer, P., Lockwood, J.P., Becker, N., Phipps, S., Todd, C.S., 2000. Significance of serpentine mud
788 volcanism in convergent margins. Geol. Soc. Am. Spec. Pap. 349;, 35–51.
789 https://doi.org/10.1130/0-8137-2349-3.35

790 Fryer, P., Mottl, M.J., 1992. 19. Lithology, Mineralogy, and Origin of Serpentine Muds Recovered
791 From Conical and Torishima Forearc Seamounts: Results of Leg 125 Drilling. Proc. Ocean Drill.
792 Program, Sci. Results 125, 343–362. https://doi.org/10.2973/odp.proc.sr.125.126.1992

793 Fryer, P., Wheat, G., Williams, T., Albers, E., Bekins, B., Debret, B., Deng, J., Dong, Y.,
794 Eickenbusch, P., Frery, E., Ichiyama, Y., Johnson, K., Johnston, R., Kevorkian, R., Kruz, W.,
795 Magalhaes, V., Mantovanelli, S., Menapace, W., Menzies, C., Michibayashi, K., Moyer, C.,
796 Mullane, K., Park, J.-W., Price, R., Ryan, J., Shervais, J., Sissmann, O., Suzuki, S., Takai, K.,
797 Walter, B., Zhang, R., 2018. Mariana Convergent Margin and South Chamorro Seamount. Proc.
798 Int. Ocean Discov. Progr. 366. https://doi.org/https://doi.org/10.14379/iodp.proc.366.2018

799 Geldmacher, J., Hoernle, K., van den Bogaard, P., Hauff, F., Klügel, A., 2008. Age and geochemistry
800 of the central American forearc basement (DSDP Leg 67 and 84): Insights into mesozoic arc
801 volcanism and seamount accretion on the fringe of the Caribbean LIP. J. Petrol. 49, 1781–1815.
802 https://doi.org/10.1093/petrology/egn046

803 Gerya, T. V., Stöckhert, B., Perchuk, A.L., 2002. Exhumation of high-pressure metamorphic rocks in a
804 subduction channel: A numerical simulation. Tectonics 21, 6-1-6–19.
805 https://doi.org/10.1029/2002TC001406

806 Godard, M., Lagabrielle, Y., Alard, O., Harvey, J., 2008. Geochemistry of the highly depleted
807 peridotites drilled at ODP Sites 1272 and 1274 (Fifteen-Twenty Fracture Zone, Mid-Atlantic
808 Ridge): Implications for mantle dynamics beneath a slow spreading ridge. Earth Planet. Sci. Lett.
809 267, 410–425. https://doi.org/10.1016/j.epsl.2007.11.058

810 Groppo, C., Rinaudo, C., Cairo, S., Gastaldi, D., Compagnoni, R., 2006. Micro-Raman spectroscopy
811 for a quick and reliable identification of serpentine minerals from ultramafics. Eur. J. Mineral.
812 18, 319–329. https://doi.org/10.1127/0935-1221/2006/0018-0319

813 Guillot, S., Hattori, K.H., De Sigoyer, J., 2000. Mantle wedge serpentinization and exhumation of
814 eclogites: Insights from eastern Ladakh, northwest Himalaya. Geology 28, 199–202.
815 https://doi.org/10.1130/0091-7613(2000)28<199:MWSAEO>2.0.CO;2

816 Harry, D.L., Ferguson, J.F., 1991. Bounding the state of stress at oceanic convergent zones.
817 Tectonophysics 187, 305–314. https://doi.org/10.1016/0040-1951(91)90426-S

818 Hattori, K., Takahashi, Y., Guillot, S., Johanson, B., 2005. Occurrence of arsenic (V) in forearc mantle
819 serpentinites based on X-ray absorption spectroscopy study. Geochim. Cosmochim. Acta 69,
820 5585–5596. https://doi.org/10.1016/j.gca.2005.07.009

821 Hattori, K.H., Guillot, S., 2007. Geochemical character of serpentinites associated with high- to
822 ultrahigh-pressure metamorphic rocks in the Alps, Cuba, and the Himalayas: Recycling of
823 elements in subduction zones. Geochemistry Geophys. Geosystems 8, Q09010.
824 https://doi.org/10.1029/2007GC001594

825 Hilairet, N., Reynard, B., 2009. Stability and dynamics of serpentinite layer in subduction zone.
826 Tectonophysics 465, 24–29. https://doi.org/10.1016/j.tecto.2008.10.005

827 Hilairet, N., Reynard, B., Wang, Y., Daniel, I., Merkel, S., Nishiyama, N., Petitgirard, S., 2007. High-
828 pressure creep of serpentine, interseismic deformation, and initiation of subduction. Science (80-.
829). 318, 1910–1913. https://doi.org/10.1126/science.1148494

830 Honda, S., Gerya, T., Zhu, G., 2010. A simple three-dimensional model of thermo-chemical
831 convection in the mantle wedge. Earth Planet. Sci. Lett. 290, 311–318.
832 https://doi.org/10.1016/j.epsl.2009.12.027

833 Hulme, S.M., Wheat, C.G., Fryer, P., Mottl, M.J., 2010. Pore water chemistry of the Mariana
834 serpentinite mud volcanoes: A window to the seismogenic zone. Geochemistry, Geophys.
835 Geosystems 11. https://doi.org/10.1029/2009GC002674

836 Inglis, E.C., Debret, B., Burton, K.W., Millet, M.A., Pons, M.L., Dale, C.W., Bouilhol, P., Cooper,
837 M., Nowell, G.M., McCoy-West, A.J., Williams, H.M., 2017. The behavior of iron and zinc
838 stable isotopes accompanying the subduction of mafic oceanic crust: A case study from Western
839 Alpine ophiolites. Geochemistry, Geophys. Geosystems 18, 2562–2579.
840 https://doi.org/10.1002/2016GC006735

841 Jöns, N., Bach, W., Klein, F., 2010. Magmatic influence on reaction paths and element transport
842 during serpentinization. Chem. Geol. 274, 196–211.
843 https://doi.org/10.1016/j.chemgeo.2010.04.009

844 Kahl, W.A., Jöns, N., Bach, W., Klein, F., Alt, J.C., 2015. Ultramafic clasts from the South Chamorro
845 serpentine mud volcano reveal a polyphase serpentinization history of the Mariana forearc
846 mantle. Lithos 227, 99–147. https://doi.org/10.1016/j.lithos.2015.03.015

847 Kamimura, A., Kasahara, J., Shinohara, M., Hino, R., Shiobara, H., Fujie, G., Kanazawa, T., 2002.
848 Crustal structure study at the Izu-Bonin subduction zone around 31°N: Implications of
849 serpentinized materials along the subduction plate boundary. Phys. Earth Planet. Inter. 132, 105–
850 129. https://doi.org/10.1016/S0031-9201(02)00047-X

851 Kashefi, K., Lovley, D.R., 2003. Extending the upper temperature limit for life. Science (80-.). 301,
852 934. https://doi.org/10.1126/science.1086823

853 Kawahara, H., Endo, S., Wallis, S.R., Nagaya, T., Mori, H., Asahara, Y., 2016. Brucite as an
854 important phase of the shallow mantle wedge: Evidence from the Shiraga unit of the Sanbagawa
855 subduction zone, SW Japan. Lithos 254–255, 53–66. https://doi.org/10.1016/j.lithos.2016.02.022

856 Kelley, K.D., Wilkinson, J.J., Chapman, J.B., Crowther, H.L., Weiss, D.J., 2009. Zinc isotopes in
857 sphalerite from base metal deposits in the Red Dog district, northern Alaska. Econ. Geol. 104,
858 767–773. https://doi.org/10.2113/gsecongeo.104.6.767

859 Kerrick, D.M., Connolly, J.A.D., 2001. Metamorphic devolatilization of subducted oceanic
860 metabasalts: Implications for seismicity, arc magmatism and volatile recycling. Earth Planet. Sci.
861 Lett. 189, 19–29. https://doi.org/10.1016/S0012-821X(01)00347-8

862 King, R.L., Bebout, G.E., Moriguti, T., Nakamura, E., 2006. Elemental mixing systematics and Sr-Nd
863 isotope geochemistry of mélange formation: Obstacles to identification of fluid sources to arc
864 volcanics. Earth Planet. Sci. Lett. 246, 288–304. https://doi.org/10.1016/j.epsl.2006.03.053

865 Klein, F., Bach, W., Humphris, S.E., Kahl, W.A., Jöns, N., Moskowitz, B., Berquó, T.S., 2014.

866 Magnetite in seafloor serpentinite-Some like it hot. Geology 42, 135–138.
867 https://doi.org/10.1130/G35068.1

868 Kodolányi, J., Pettke, T., 2011. Loss of trace elements from serpentinites during fluid-assisted
869 transformation of chrysotile to antigorite - An example from Guatemala. Chem. Geol. 284, 351–
870 362. https://doi.org/10.1016/j.chemgeo.2011.03.016

871 Kodolanyi, J., Pettke, T., Spandler, C., Kamber, B.S., Gmeling, K., 2011. Geochemistry of Ocean
872 Floor and Fore-arc Serpentinites: Constraints on the Ultramafic Input to Subduction Zones. J.
873 Petrol. 53, 235–270. https://doi.org/10.1093/petrology/egr058

874 Maekawa, H., Shozul, M., Ishii, T., Fryer, P., Pearce, J.A., 1993. Blueschist Metamorphism in an
875 Active Subduction Zone. Nature 364, 520–523. https://doi.org/10.1038/364520a0

876 Mottl, M.J., Komor, S.C., Fryer, P., Moyer, C.L., 2003. Deep-slab fluids fuel extremophilic Archaea
877 on a Mariana forearc serpentinite mud volcano: Ocean drilling program leg 195. Geochemistry,
878 Geophys. Geosystems 4. https://doi.org/10.1029/2003GC000588

879 Murata, K., Maekawa, H., Yokose, H., Yamamoto, K., Fujioka, K., Ishii, T., Chiba, H., Wada, Y.,
880 2009. Significance of serpentinization of wedge mantle peridotites beneath Mariana forearc,
881 western Pacific. Geosphere 5, 90–104. https://doi.org/10.1130/GES00213.1

882 Nagaya, T., Walker, A.M., Wookey, J., Wallis, S.R., Ishii, K., Kendall, J.M., 2016. Seismic evidence
883 for flow in the hydrated mantle wedge of the Ryukyu subduction zone. Sci. Rep. 6.
884 https://doi.org/10.1038/srep29981

885 Niu, Y., 2004. Bulk-rock Major and Trace Element Compositions of Abyssal Peridotites: Implications
886 for Mantle Melting, Melt Extraction and Post-melting Processes Beneath Mid-Ocean Ridges. J.
887 Petrol. 45, 2423–2458. https://doi.org/10.1093/petrology/egh068

888 Oakley, A.J., 2008. A multi-channel seismic and bathymeric investigation of the central Mariana
889 convergent margin. University of Hawaii.

890 Pabst, S., Zack, T., Savov, I.P., Ludwig, T., Rost, D., Vicenzi, E.P., 2011. Evidence for boron

891 incorporation into the serpentine crystal structure. Am. Mineral. 96, 1112–1119.
892 https://doi.org/10.2138/am.2011.3709

893 Parkinson, I.J., Pearce, J.A., 1998. Peridotites from the Izu-Bonin-Mariana forearc (ODP Leg 125):
894 evidence for mantle melting and melt-mantle interaction in a supra-subduction zone setting. J.
895 Petrol. 39, 1577–1618. https://doi.org/10.1093/petroj/39.9.1577

896 Paulick, H., Bach, W., Godard, M., De Hoog, J.C.M., Suhr, G., Harvey, J., 2006. Geochemistry of
897 abyssal peridotites (Mid-Atlantic Ridge, 15°20′N, ODP Leg 209): Implications for fluid/rock
898 interaction in slow spreading environments. Chem. Geol. 234, 179–210.
899 https://doi.org/10.1016/j.chemgeo.2006.04.011

900 Pearce, J.A., Barker, P.F., Edwards, S.J., Parkinson, I.J., Leat, P.T., 2000. Geochemistry and tectonic
901 significance of peridotites from the South Sandwich arc-basin system, South Atlantic. Contrib. to
902 Mineral. Petrol. 139, 36–53. https://doi.org/10.1007/s004100050572

903 Peters, D., Bretscher, A., John, T., Scambelluri, M., Pettke, T., 2017. Fluid-mobile elements in
904 serpentinites: Constraints on serpentinisation environments and element cycling in subduction
905 zones. Chem. Geol. 466, 654–666. https://doi.org/10.1016/j.chemgeo.2017.07.017

906 Plümper, O., King, H., Geisler, T., Liu, Y., Pabst, S., Savov, I.P., Rost, D., Zack, T., 2017. Subduction
907 zone forearc serpentinites as incubators for deep microbial life? Proceedings of the National
908 Academy of Sciences 114, 4323-4329

909 Pons, M.-L., Debret, B., Bouilhol, P., Delacour, A., Williams, H., 2016. Zinc isotope evidence for
910 sulfate-rich fluid transfer across subduction zones. Nat. Commun. 7, 13794.
911 https://doi.org/10.1038/ncomms13794

912 Reynard, B., 2013. Serpentine in active subduction zones. Lithos.
913 https://doi.org/10.1016/j.lithos.2012.10.012

914 Ribeiro, J.M., Lee, C.T.A., 2017. An imbalance in the deep water cycle at subduction zones: The
915 potential importance of the fore-arc mantle. Earth Planet. Sci. Lett. 479, 298–309.

916 https://doi.org/10.1016/j.epsl.2017.09.018

917 Rouméjon, S., Cannat, M., Agrinier, P., Godard, M., Andreani, M., 2014. Serpentinization and fluid
918 pathways in tectonically exhumed peridotites from the southwest Indian ridge (62-65°E). J.
919 Petrol. 56, 703–734. https://doi.org/10.1093/petrology/egv014

920 Rüpke, L.H., Morgan, J.P., Hort, M., Connolly, J.A.D., 2004. Serpentine and the subduction zone
921 water cycle. Earth Planet. Sci. Lett. 223, 17–34. https://doi.org/10.1016/j.epsl.2004.04.018

922 Saccocia, P. J., Seewald, J. S., & Shanks III, W. C. (2009). Oxygen and hydrogen isotope fractionation
923 in serpentine–water and talc–water systems from 250 to 450 C, 50 MPa. *Geochimica et*
924 *Cosmochimica Acta*, *73*(22), 6789-6804.Sakai, R., Kusakabe, M., Noto, M., Ishii, T., 1990.
925 Origin of waters responsible for serpentinization of the Izu-Ogasawara-Mariana forearc
926 seamounts in view of hydrogen and oxygen isotope ratios. Earth Planet. Sci. Lett. 100, 291–303.
927 https://doi.org/10.1016/0012-821X(90)90192-Z

928 Savov, I.P., Guggino, S., Ryan, J.G., Fryer, P., Mottl, M.J., 2004. Geochemistry of serpentinite muds
929 and metamorphic rocks from the Mariana forearc, ODP Sites 1200 and 778-779, South
930 Chamorro and Conical Seamounts, In Shinohara, M., Salisbury, M.H., and Richter, C. (Eds.),
931 Proc. ODP, Sci. Results.

932 Savov, I.P., Ryan, J.G., D'Antonio, M., Fryer, P., 2007. Shallow slab fluid release across and along
933 the Mariana arc-basin system: Insights from geochemistry of serpentinized peridotites from the
934 Mariana fore arc. J. Geophys. Res. 112, B09205. https://doi.org/10.1029/2006JB004749

935 Savov, I.P., Ryan, J.G., D'Antonio, M., Kelley, K., Mattie, P., 2005. Geochemistry of serpentinized
936 peridotites from the Mariana Forearc Conical Seamount, ODP Leg 125: Implications for the
937 elemental recycling at subduction zones. Geochemistry Geophys. Geosystems 6, Q04J15.
938 https://doi.org/10.1029/2004GC000777

939 Scambelluri, M., Müntener, O., Ottolini, L., Pettke, T.T., Vannucci, R., 2004. The fate of B, Cl and Li
940 in the subducted oceanic mantle and in the antigorite breakdown fluids. Earth Planet. Sci. Lett.

222, 217–234. https://doi.org/10.1016/j.epsl.2004.02.012

Schwartz, S., Allemand, P., Guillot, S., 2001. Numerical model of the effect of serpentinites on the exhumation of eclogitic rocks: Insights from the Monviso ophiolitic massif (Western Alps). Tectonophysics 342, 193–206. https://doi.org/10.1016/S0040-1951(01)00162-7

Schwartz, S., Guillot, S., Reynard, B., Lafay, R., Debret, B., Nicollet, C., Lanari, P., Auzende, A.L., 2013. Pressure-temperature estimates of the lizardite/antigorite transition in high pressure serpentinites. Lithos 178, 197–210. https://doi.org/10.1016/j.lithos.2012.11.023

Schwarzenbach, E.M., Caddick, M.J., Beard, J.S., Bodnar, R.J., 2016. Serpentinization, element transfer, and the progressive development of zoning in veins: evidence from a partially serpentinized harzburgite. Contrib. to Mineral. Petrol. 171, 1–22. https://doi.org/10.1007/s00410-015-1219-3

Sharp, Z.D., 1990. A laser-based microanalytical method for the in situ determination of oxygen isotope ratios of silicates and oxides. Geochim. Cosmochim. Acta 54, 1353–1357. https://doi.org/10.1016/0016-7037(90)90160-M

Snyder, G.T., Savov, I.P., Muramatsu, Y., 2005. 5 . Iodine and Boron in Mariana serpentinite mud volcanoes (ODP Legs 125 and 195): implications for forearc processes and subduction revycling. Proc. Ocean Drill. Program, Sci. Results 195, 1–18. https://doi.org/10.2973/odp.proc.sr.195.102.2005

Sun, S., McDonough, W.F., 1989. Chemical and isotopic systematics of oceanic basalts: implications for mantle composition and processes. Geol. Soc. London, Spec. Publ. 42, 313–345. https://doi.org/10.1144/GSL.SP.1989.042.01.19

Tamblyn, R., Hand, M., Zack, T., Kelsey, D., Morrissey, L., Pabst, S., Savov, I. P, 2018. Metamorphic conditions of blueschist erupted from serpentinite mud volcanism in the Mariana forearc, EGU Meeting, Vienna

Taylor, B., Smoot, N.C., 1984. Morphology of Bonin fore-arc submarine canyons. Geology.

https://doi.org/10.1130/0091-7613(1984)12<724:MOBFSC>2.0.CO;2

Thiel, V., Peckmann, J., Seifert, R., Wehrung, P., Reitner, J., Michaelis, W., 1999. Highly isotopically depleted isoprenoids: molecular markers for ancient methane venting. Geochim. Cosmochim. Acta 63, 3959–3966. https://doi.org/10.1016/S0016-7037(99)00177-5

Valley, J.W., Kitchen, N., Kohn, M.J., Niendorf, C.R., Spicuzza, M.J., 1995. UWG-2, a garnet standard for oxygen isotope ratios: Strategies for high precision and accuracy with laser heating. Geochim. Cosmochim. Acta 59, 5223–5231. https://doi.org/10.1016/0016-7037(95)00386-X

Van Keken, P.E., Hacker, B.R., Syracuse, E.M., Abers, G.A., 2011. Subduction factory: 4. Depth-dependent flux of H2O from subducting slabs worldwide. J. Geophys. Res. Solid Earth 116. https://doi.org/10.1029/2010JB007922

Vils, F., Müntener, O., Kalt, A., Ludwig, T., 2011. Implications of the serpentine phase transition on the behaviour of beryllium and lithium–boron of subducted ultramafic rocks. Geochim. Cosmochim. Acta 75, 1249–1271. https://doi.org/10.1016/j.gca.2010.12.007

Wada, I., Wang, K., He, J., Hyndman, R.D., 2008. Weakening of the subduction interface and its effects on surface heat flow, slab dehydration, and mantle wedge serpentinization. J. Geophys. Res. Solid Earth 113. https://doi.org/10.1029/2007JB005190

Wenner, D.B., Taylor, H.P., 1971. Temperatures of serpentinization of ultramafic rocks based on O18/O16 fractionation between coexisting serpentine and magnetite. Contrib. to Mineral. Petrol. 32, 165–185. https://doi.org/10.1007/BF00643332

Wilkin, R.T., Barnes, H.L., 1997. Formation processes of framboidal pyrite. Geochim. Cosmochim. Acta 61, 323–339. https://doi.org/10.1016/S0016-7037(96)00320-1

Wunder, B., Wirth, R., Gottschalk, M., 2001. Antigorite: Pressure and temperature dependence of polysomatism and water content. Eur. J. Mineral. 13, 485–495. https://doi.org/10.1127/0935-1221/2001/0013-0485

991 **Figure Captions**

992 Fig. 1: Bathymetry map of the Mariana subduction system showing the locations of Yinazao,
993 Fantangisña and Asùt Tesoru drilled during IODP Exp. 366 as well as Conical and South Chamorro
994 that were drilled during previous ODP legs.

995 Fig. 2: Representative core images of the main lithostratigraphic units observed at Yinazao,
996 Fantangisña and Asùt Tesoru flanks or summits. (a) Core image of the upper level unit recovered at
997 the site U1492A (Yinazao summit, section 1H2-99/139cm). The uppermost units of the mud-volcano
998 is made of red-brown pelagic mud containing carbonated serpentinite breccia and weathered
999 serpentinites clasts (brown weathering). (b) Core image of the contact between upper and lower level
1000 units at the Site U1496A (Asùt Tesoru summit, section 1F1-1/41cm). The uppermost units of the mud-
1001 volcano is made of red-brown pelagic mud containing partly weathered serpentinite clasts. Note that
1002 the clast displays a carbonated and brown weathering crust toward to the core. The clast itself is also
1003 rimed by a halo of Blue-serpentinite while the core correspond to a Liz-serpentinite. The square
1004 indicates the localization of the macroscopic picture and thin section observations presented in
1005 Appendix A. The lower unit is made of blue-grey serpentinite mud containing serpentinite clasts of
1006 various size. (c) Core image of the lower level unit recovered at the Site 1492A (Yinazao summit,
1007 section 4F2-50/90cm). The lower unit is made of blue-grey serpentinite mud containing serpentinite
1008 clasts of various size. (d) Core image of a large clast of 40 cm long recovered at the Site 1498B
1009 (Fantangisña flank, section 3R3, 38-78cm).

1010 Fig. 3: Photomicrographs (a: crossed polarized light; b and c: plane polarized light), back scattered
1011 electron image and Raman spectra of the carbonated (a) and blue (b-d) serpentinites recovered at the
1012 Yinazao mud volcano (photo taken by the Shipboard Scientists, 2018). (a) Carbonated breccia
1013 (shipboard sample U1491B-2H5-85/88) showing dismembered crack-seal like veins (mainly made of
1014 chrysotile, Ctl) embedded into a calcite (Cal) matrix. (b) Mesh textures with a pale blue colour
1015 (sample M7) and corresponding Raman spectra. The meshes centres are replaced by opaque
1016 aggregates composed of sulfide (pyrite) and brucite ± serpentine. Raman spectra of mesh rim (black
1017 line) and core (grey line) are mixtures between serpentine and brucite. In the high frequency region,

1018 the core of the mesh is mainly dominated by brucite. White square: localisation of the Fig. 2s. (c)
1019 Opaque vein made of pyrite crossing mesh and bastite textures (shipboard sample U1492C-8F3-
1020 108/112). The centres of the mesh and bastite textures are associated with sulfides. (d) SEM
1021 observation of a mesh core (sample M7). The core is composed of brucite lamellae with interstitial
1022 framboidal pyrite.

1023 Fig. 4: Plot of XCr vs. XMg of spinels in forearc ultramafic clasts from Yinazao, Fantangisña and
1024 Asùt Tesoru. Compositions broadly overlap with those of forearc peridotites and are more Fe- and Cr-
1025 rich with respect to abyssal peridotites (abyssal and forearc peridotite fields are from Dubois-Côté et
1026 al. (2005).

1027 Fig. 5: Major element contents and normalized cations of the different serpentine phases. (a-b)
1028 Variations of XMg (= Mg / [Fe + Mg]) and FeO with SiO_2. (c-d) Variations of Mg and Fe cations per
1029 formula unit (p.f.u.) with Si + Al cations p.f.u. The decrease of XMg and SiO_2 in serpentine
1030 crystallizing in Blue serpentinites and Liz-serpentinites reflects the presence of Si-free, Fe-rich brucite
1031 at microscale. The brucite trend intercepts SiO_2 = 0 wt% value at #Mg = 0.84. Crystallization of
1032 antigorite (Atg/Liz-serpentinites and Atg-serpentinites) is associated with the disappearance of the
1033 brucite component in serpentine analyses, an increase in SiO_2 and XMg and a decrease in FeO in
1034 serpentine.

1035 Fig. 6: Photomicrographs and corresponding Raman spectra of Liz-serpentinite recovered from Asùt
1036 Tesoru (Photomicrographs taken by the Shipboard Sci. Party, 2018). (a) Serpentine forms mesh
1037 textures with a brownish colour and preserved olivine relicts in their centres (plane polarized light,
1038 sample M19). Note the presence of euhedral and unaltered spinel on the microphotograph bottom.
1039 Mesh Raman spectra are mixed analyses of lizardite and brucite. (b) Antigorite vein with brucite and
1040 magnetite in its centre (crossed polarized light, shipboard sample U1497A-13G-CC-W 61/63). The
1041 vein crosscuts a lizardite/brucite-bearing vein.

1042 Fig. 7: Photomicrographs (crossed polarized light) and corresponding Raman spectra of the Atg/Liz-
1043 serpentinites recovered from Fantangisña and Asùt Tesoru. (a) Antigorite crystallizes as several

hundred microns long lamellae penetrating mesh textures (sample M32). Centres of the antigorite veins are composed of magnetite and brucite. Note that the centres of the mesh textures show mixed Raman spectra between lizardite and antigorite. (b) Wide vein of brucite and magnetite crosscutting relicts of mesh textures (sample M13). The mesh texture is fully recrystallized into pure antigorite where it is in contact with the vein.

Fig. 8: Photomicrographs of Atg-serpentinites recovered from Asùt Tesoru (both in crossed polarized light). (a) Antigorite lamellae with interstitial brucite and magnetite (sample M16). (b) Brucite patch associated with euhedral grains of magnetite (sample M15).

Fig. 9: Bulk rock major element composition of Mariana ultramafic clasts illustrated in (a) Al_2O_3 vs MgO/SiO_2 and (b) MgO (wt.%) vs FeO (wt.%). South Chamorro (grey crosses) and Conical (black crosses; data from Geldmacher et al., 2008; Kodolanyi et al., 2011; Parkinson and Pearce, 1998; Pearce et al., 2000; Savov et al., 2007) are shown for comparison. On Fig. 9a, the dark line represents the silicate Earth differentiation trend and the primitive mantle ratio (PM; Godard et al., 2008). Changes in whole-rock ratios of both MgO/SiO_2 and Al_2O_3/SiO_2 accompany the transition (left to right) of depleted (e.g., dunite) to enriched (e.g., lherzolith) peridotites. On Fig. 9b, the dark line represents the stoichiometric variations of olivine Fe–Mg composition. Abyssal peridotite endmembers of dunite and lherzolite (Godard et al., 2008) are shown for comparison. Note that several samples display abnormal high MgO/SiO_2 and MgO contents, such reflect the ultra-refractory compositions of the ultramafic protoliths and/or the high amount of brucite in the samples.

Fig. 10: Whole-rock trace elemental compositions of the different ultramafic clasts (Blue-, Liz-, Atg/Liz- and Atg-serpentinites). (a) and (b) patterns are normalized to chondrite and primitive mantle (PM), respectively, using normalization values from Sun and McDonough (1989). Serpentinite mud analysis is from Kodolanyi et al. (2011). Group-1 correspond to blue serpentinites with flat patterns similar to that of serpentinite muds and Group-2 correspond to blue serpentinites, Liz-, Atg/Liz- and Atg- serpentinites with U-shaped patterns.

Fig. 11: Plots of Cs/Yb vs Li* (a), As vs Sb (b) and Sr vs Zn (c) of studied ultramafic clasts. Concentrations overlap well with those of ultramafic clasts from South Chamorro (grey crosses) and Conical (black crosses; data from Geldmacher et al., 2008; Kodolanyi et al., 2011; Parkinson and Pearce, 1998; Pearce et al., 2000; Savov et al., 2007, 2005). Abyssal peridotites (white circles; data from Andreani et al., 2014; Augustin et al., 2008; Boschi et al., 2013; Delacour et al., 2008; Jöns et al., 2010; Kodolanyi et al., 2011; Niu, 2004; Paulick et al., 2006; Rouméjon et al., 2014) have consistently lower Cs/Yb and Li* contents with respect to Liz- and Atg/Liz-serpentinites. Sr (~0.4-1000 ppm) and Zn (~30-200 ppm) concentrations of abyssal peridotites and serpentinites overlap with those of the forearc but were not presented here for sake of clarity.

Fig. 12: Plot of $\delta^{18}O$ (‰) variations in ultramafic clast pore fluids vs distance to the trench (km). The $\delta^{18}O_{fluid}$ values progressively increase passing from Yinazao to Fantangisña, Asùt Tesoru, South Chamorro and Conical. M: data from Mottl et al. (2003); A: calculated $\delta^{18}O_{fluid}$ in equilibrium with antigorite below Conical by Alt and Shanks (2006).

Fig. 13: Conceptual model illustrating serpentinisation processes in relation to fluid circulation and mantle flow within the Mariana forearc. Numbers in diagram correspond to those in the P-T diagram, where pressures have been estimated according to slab/mantle interface depth estimates below the mud volcanoes (Hulme et al., 2010). As clasts from the forearc mantle are dragged down to depth (stages 1 to 3), they undergo an increase in temperature from about 200 to 400°C and the associated transformation of lizardite into antigorite. During uplift, the clasts are variably retromorphosed into blue serpentinites (stage 4).

Figure1

Click here to download high resolution image

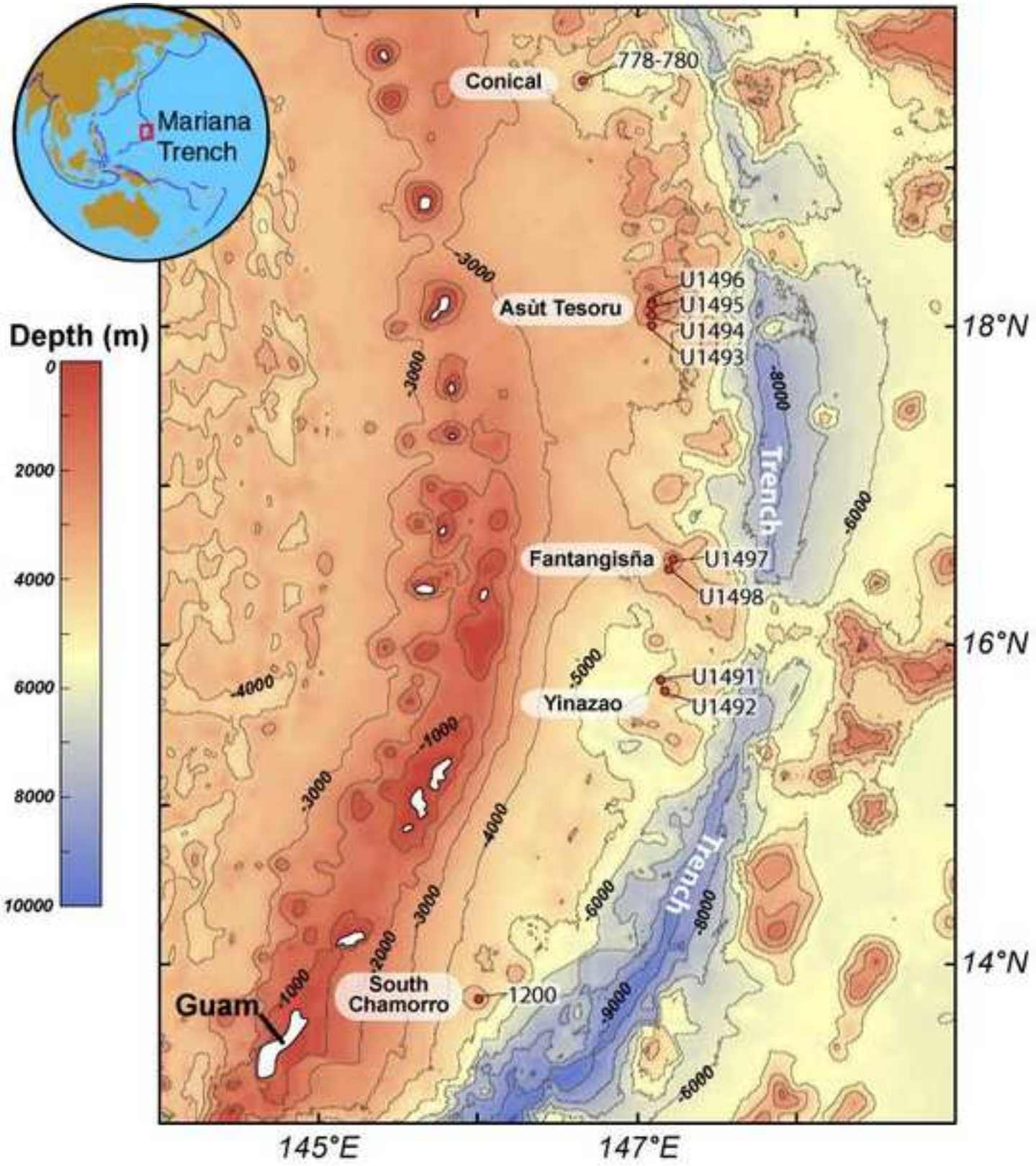

Figure2

Click here to download high resolution image

Figure3
Click here to download high resolution image

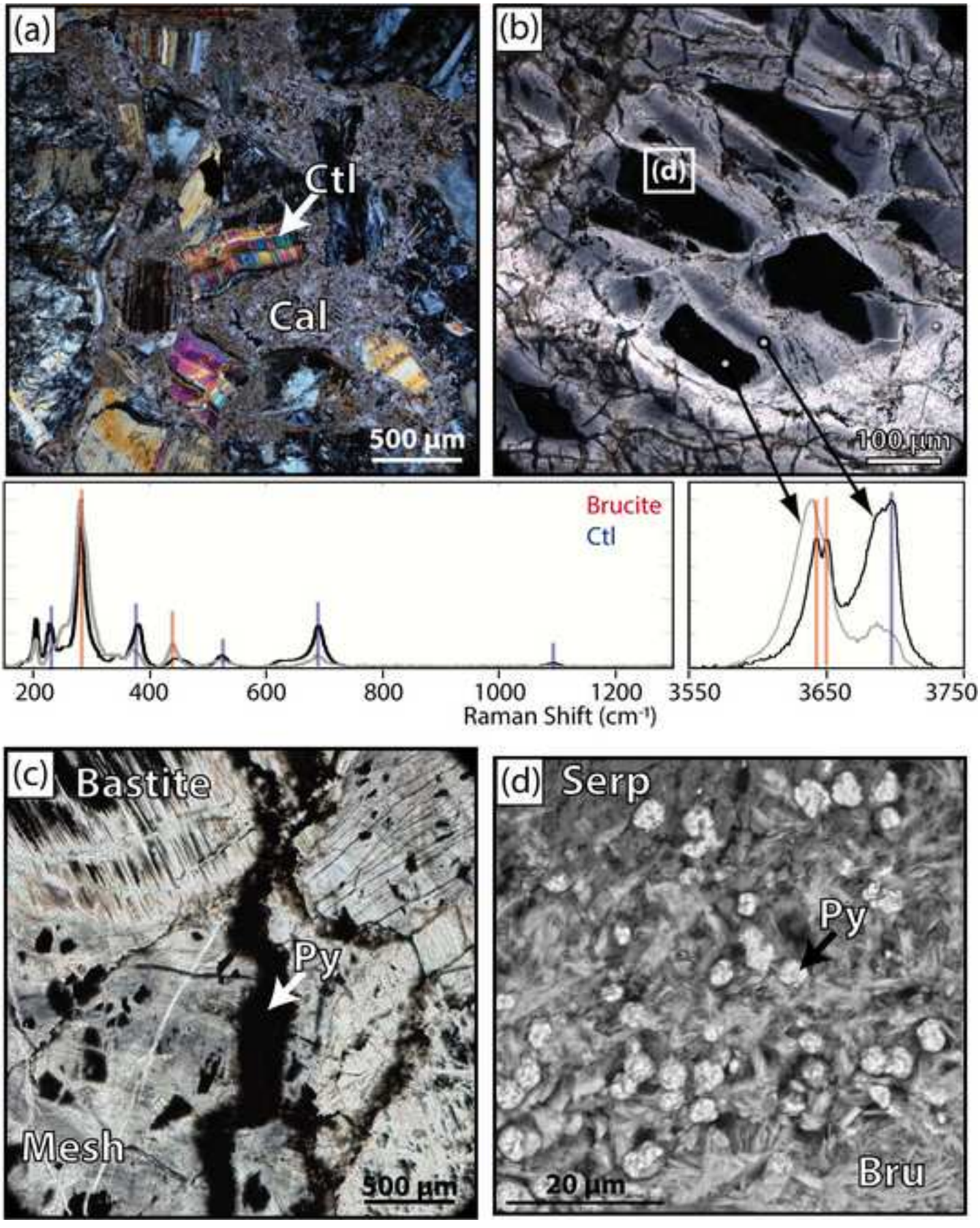

Figure4

Click here to download high resolution image

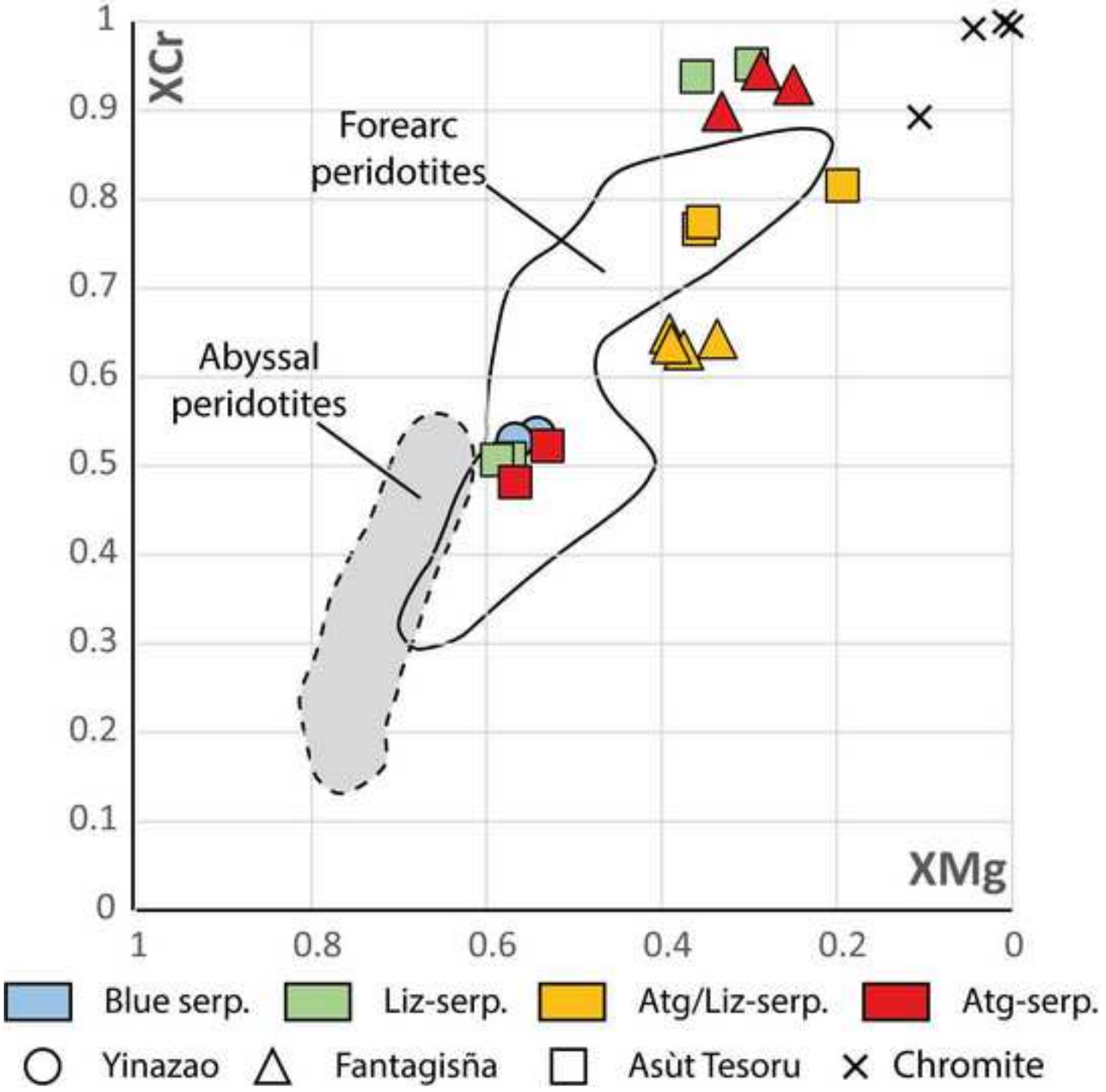

Figure5

Click here to download high resolution image

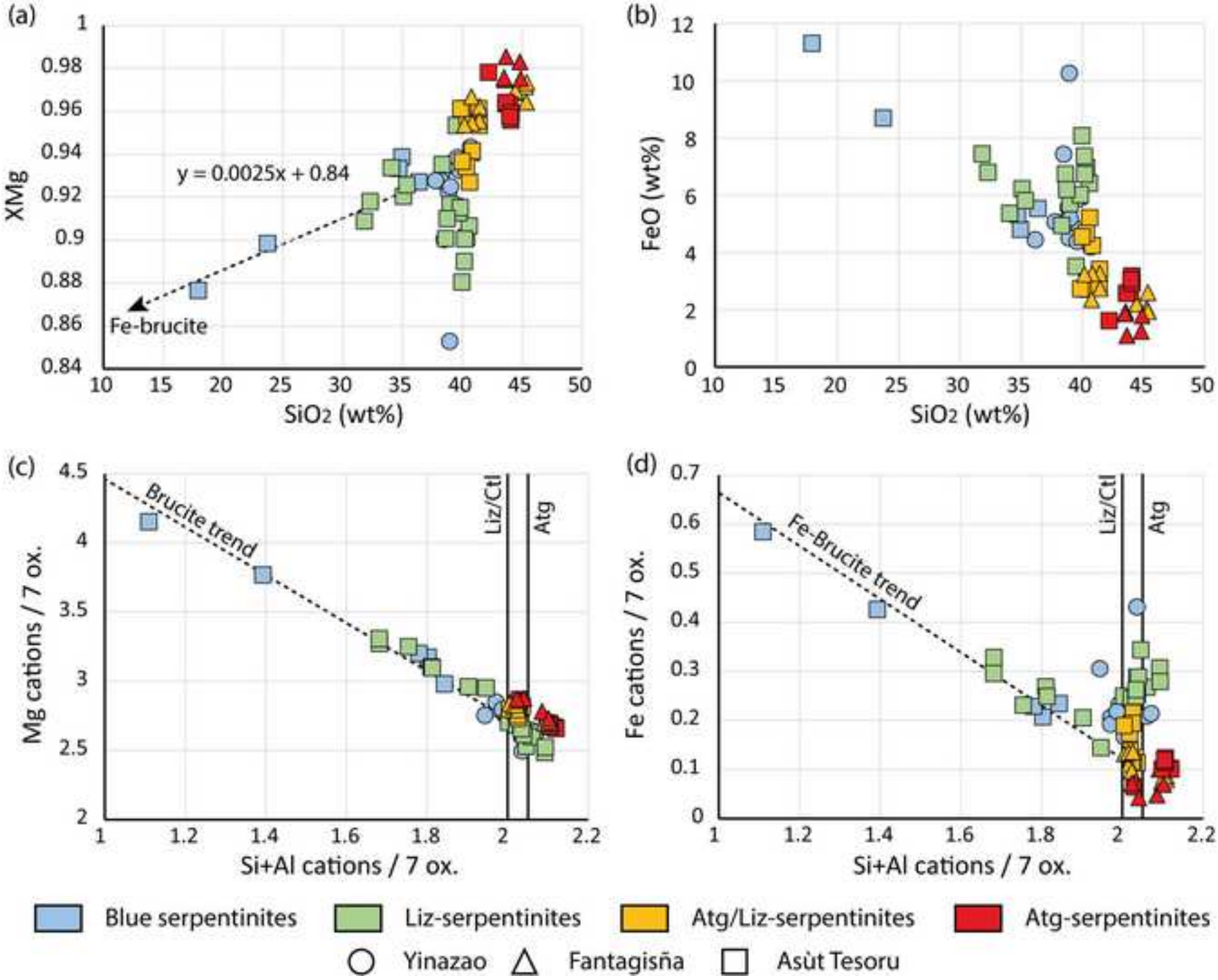

Figure6

Click here to download high resolution image

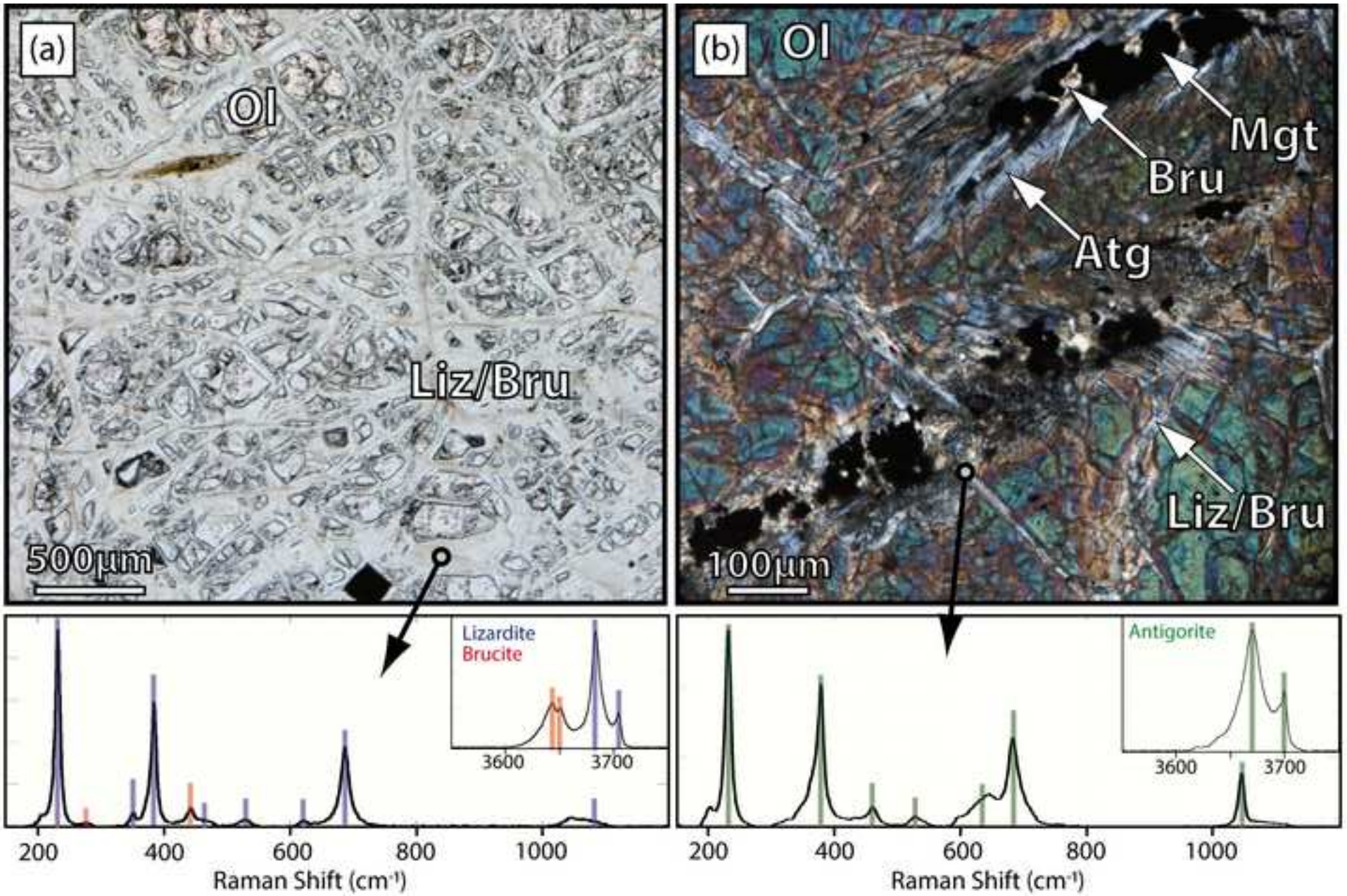

Figure7

Click here to download high resolution image

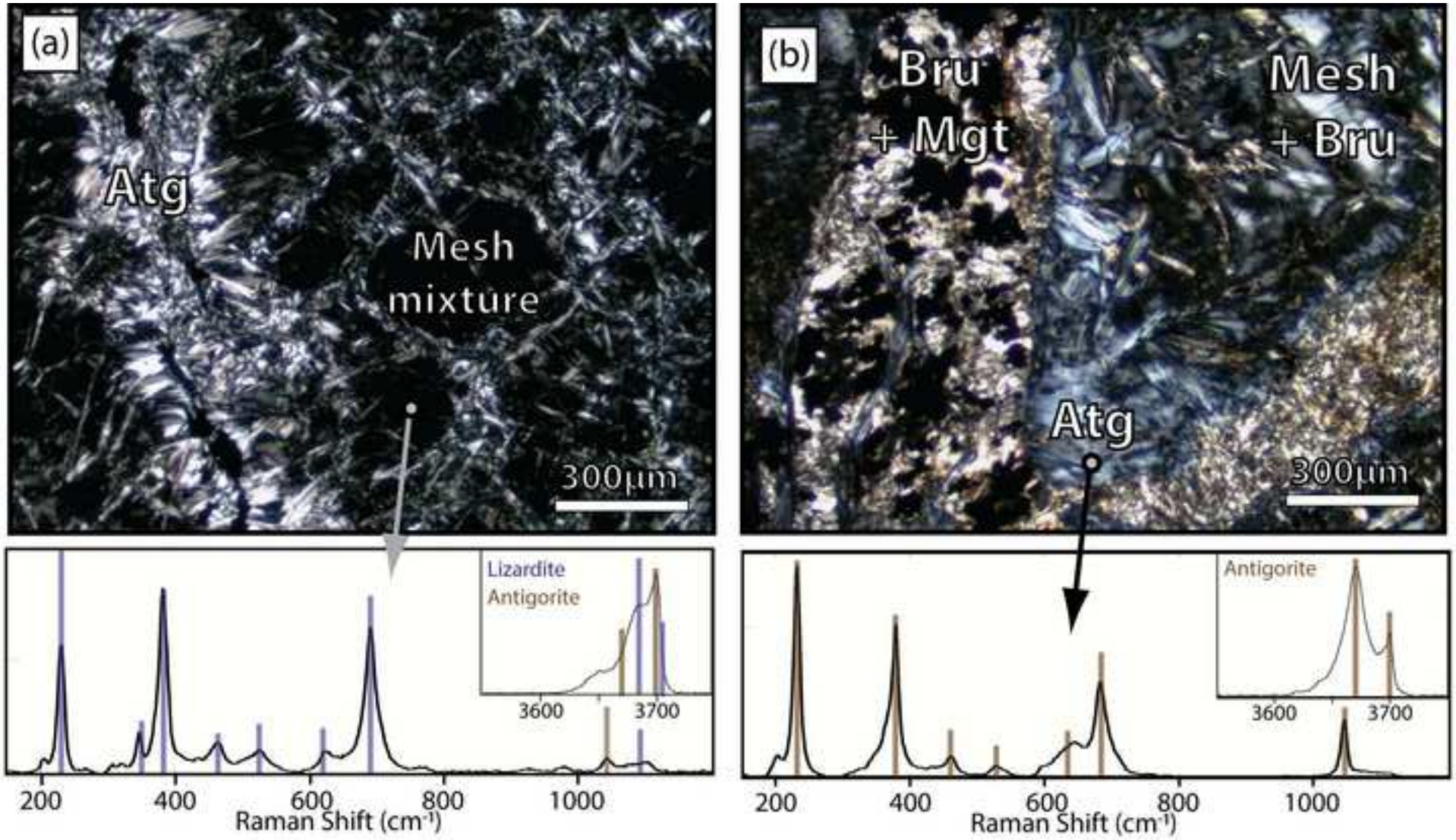

Figure8

Click here to download high resolution image

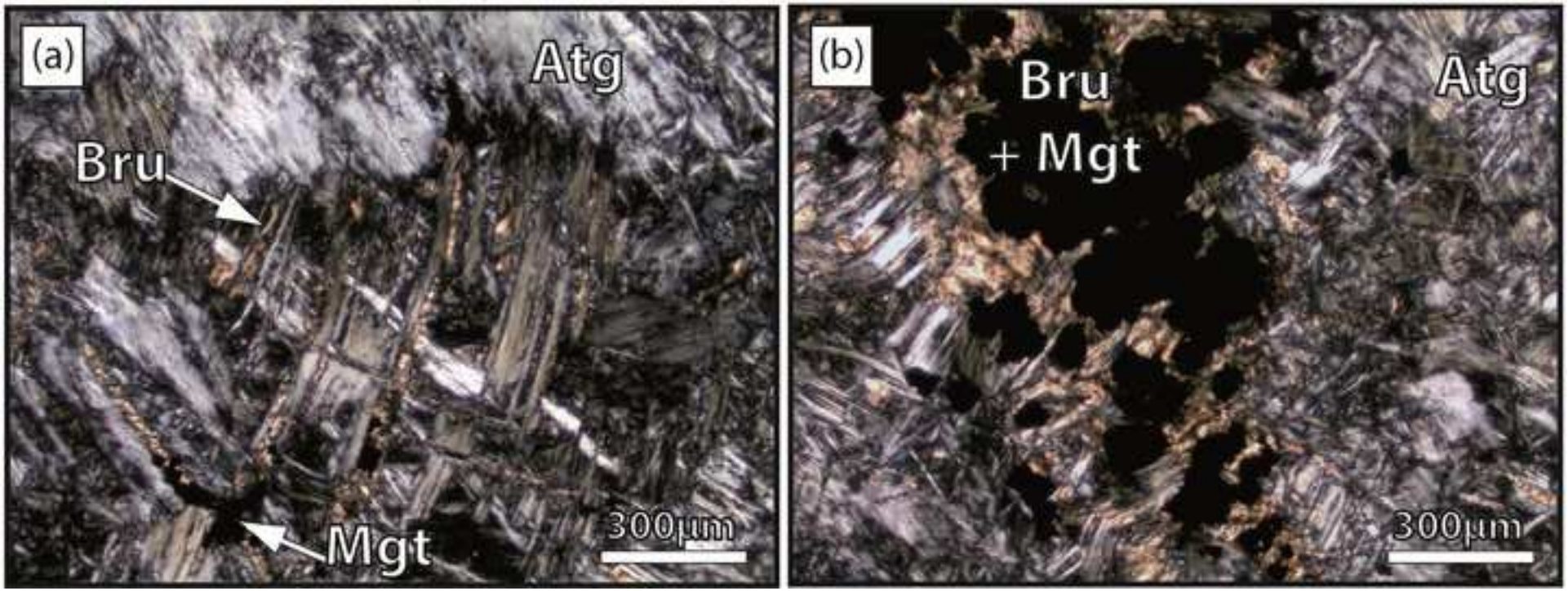

Figure9

Click here to download high resolution image

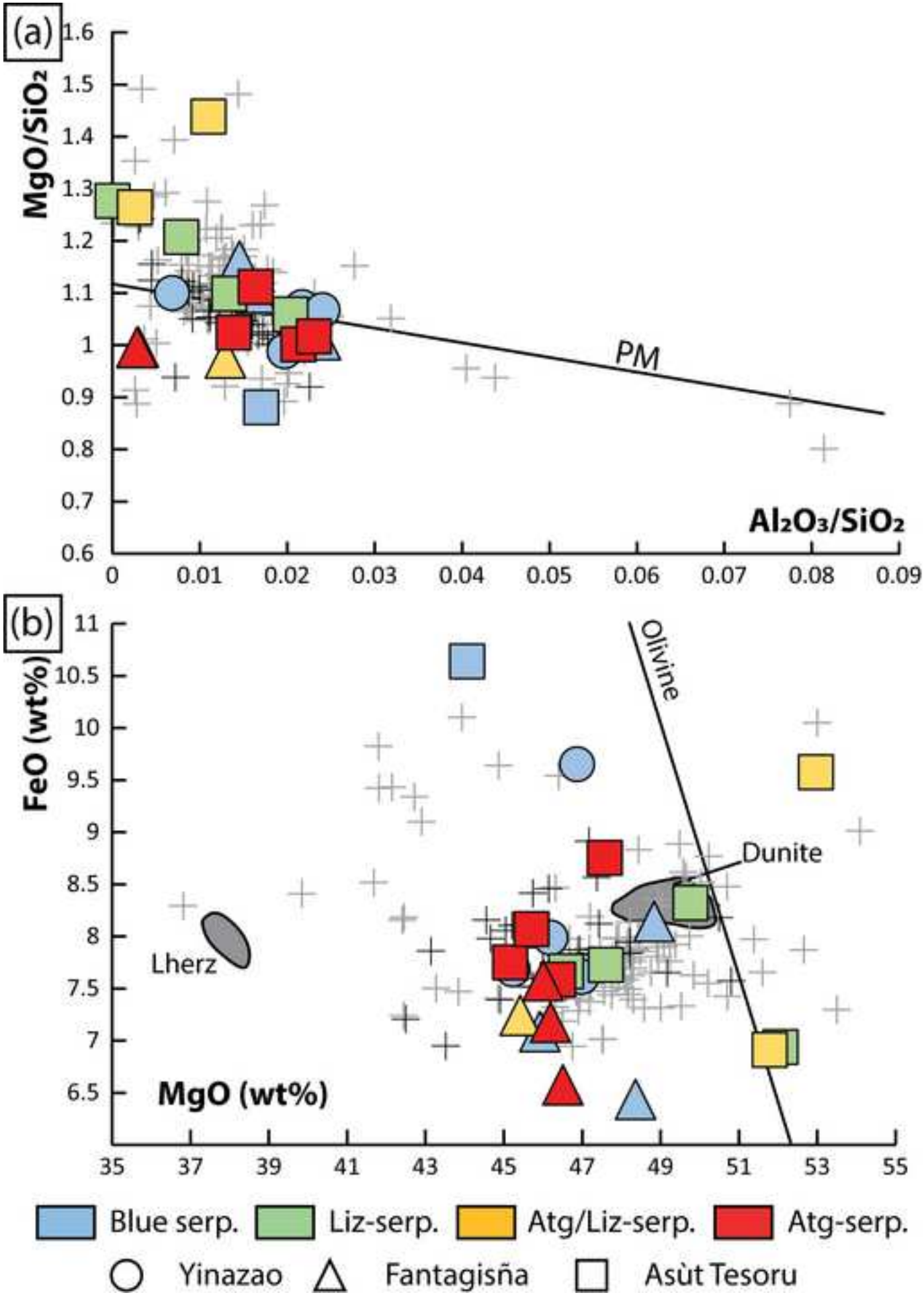

Figure10

Click here to download high resolution image

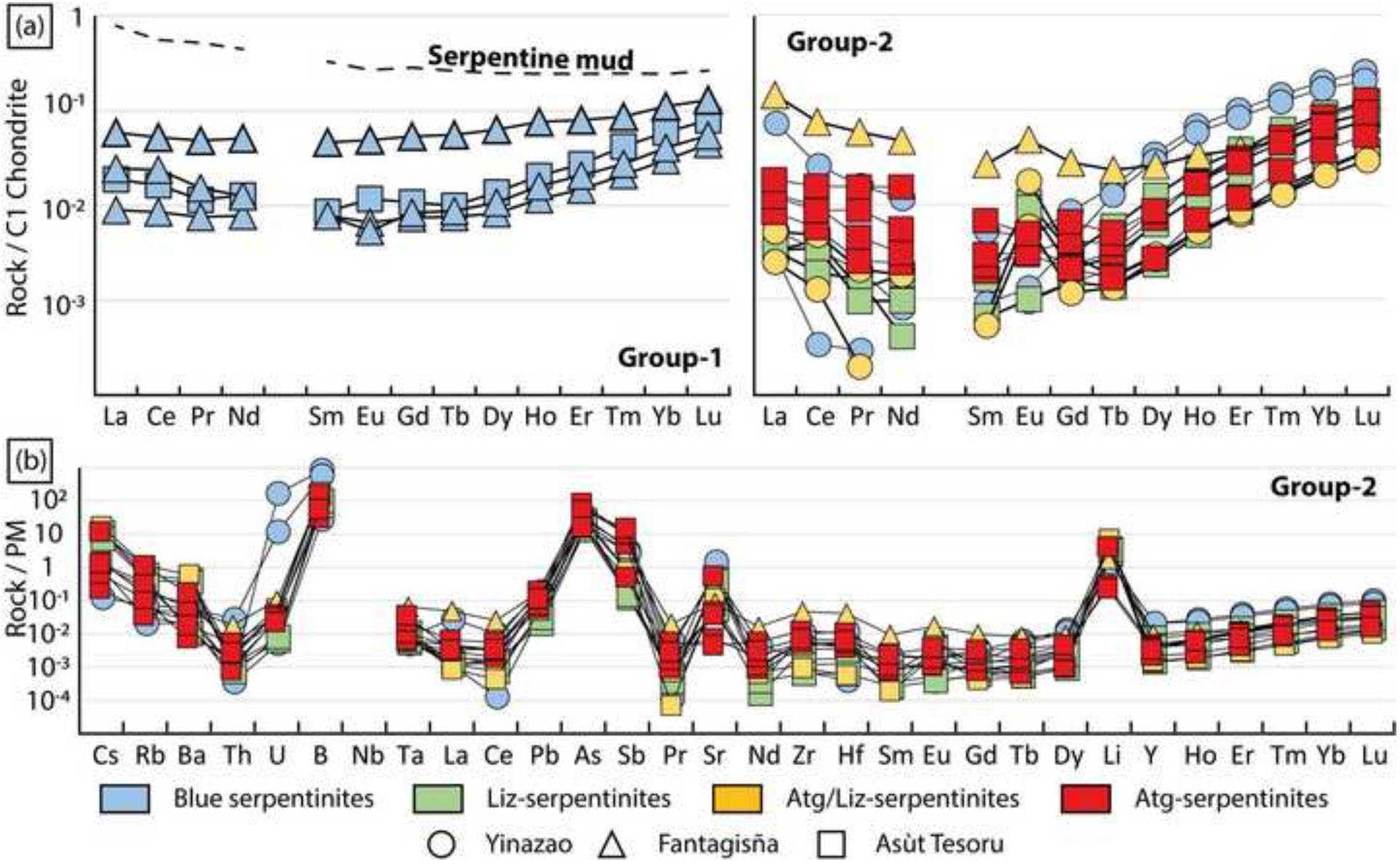

Figure11

Click here to download high resolution image

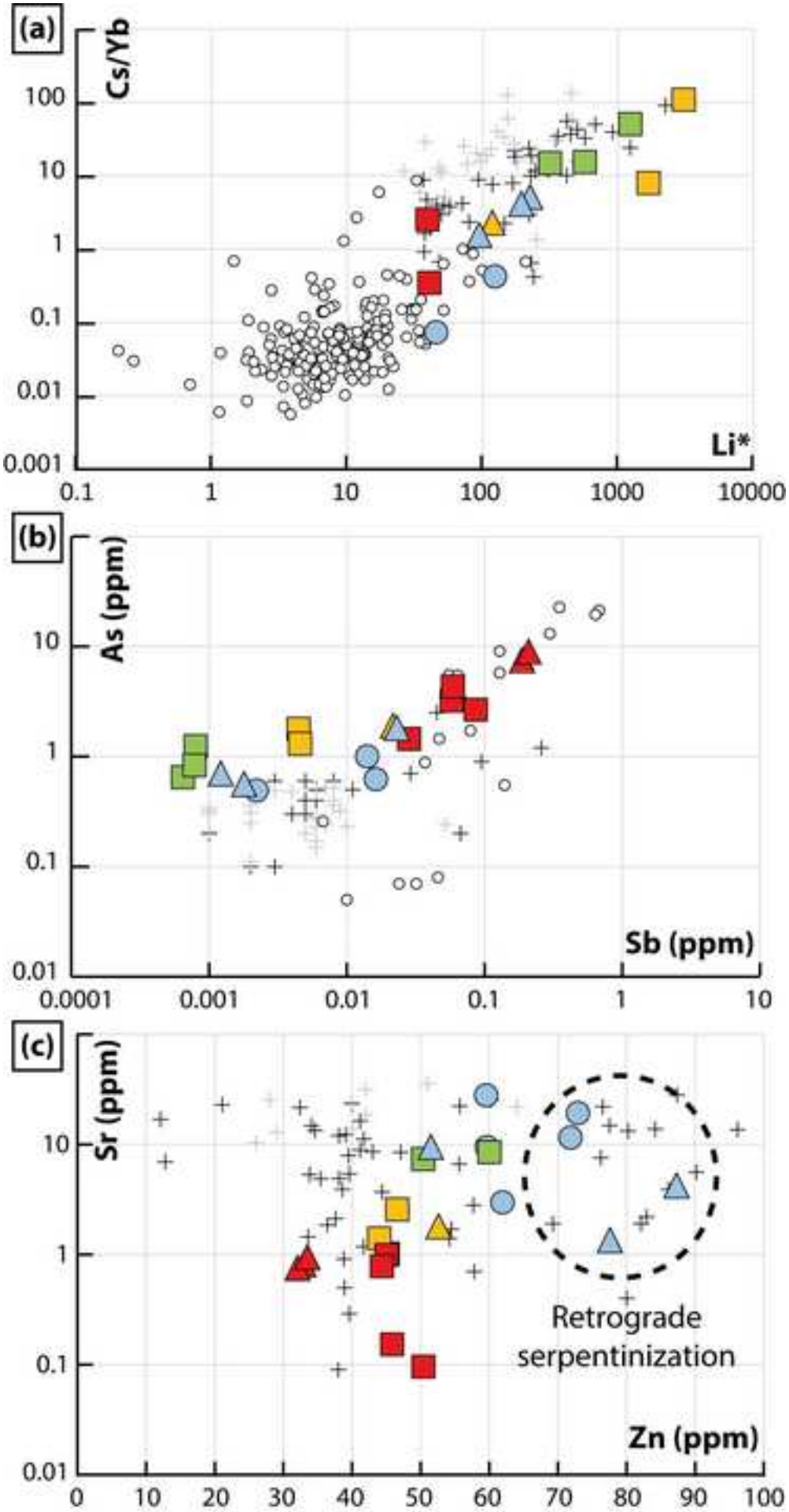

Figure12

Click here to download high resolution image

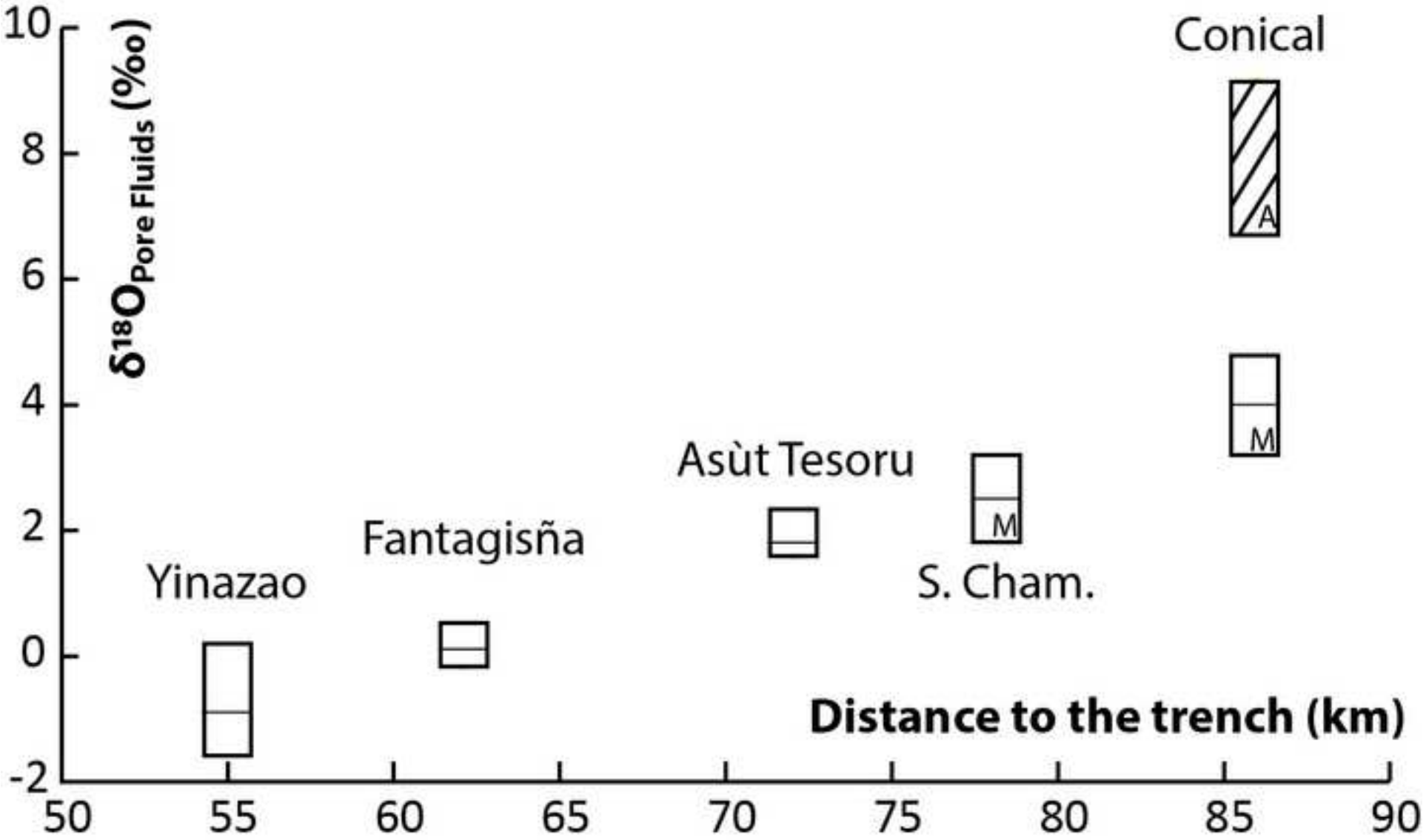

Figure13

Click here to download high resolution image

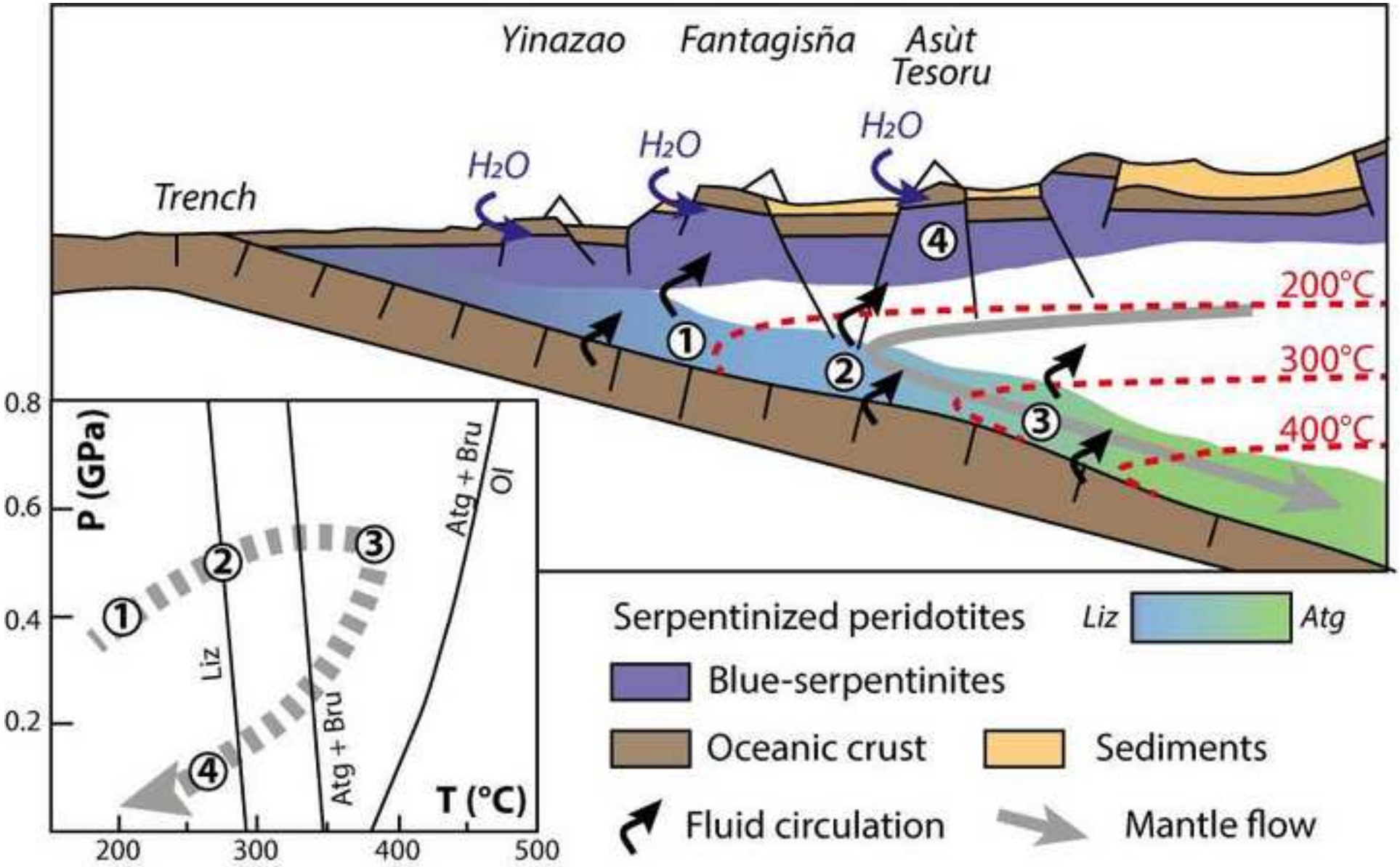

Table 1: Oxygen isotope data and resultant temperature estimates for selected samples. Pore fluid $\delta^{18}O$ are minimum, maximum and average values.

Reference	**$\delta^{18}O_{Srp}$ (‰)**	**$\delta^{18}O_{fluid}$(‰)**			**T (°C)[1]**			**$\delta 18O_{fluid}$* (‰)**	**T(°C)[1]**	**$\delta^{18}O_{Mgt}$ (‰)**	**T(°C)[2]**
		mean	min	max	mean	min	max				
Blue serpentinite											
M3	6.4	-0.9	-1.4	-0.1	183	176	194	-	-	-	-
M30	7.4 *(7.3)*	0.1	0.0	0.3	183	181	184	-	-	-	-
Liz-serpentinite											
M9	7.6	1.8	1.7	2.0	205	203	206	-	-	-	-
M10	6.8	1.8	1.7	2.0	220	218	222	-	-	-	-
Atg/Liz-serpentinite											
M12	6.1	1.8	1.7	2.0	232	230	234	4.0	276	-	-
M13	5.8	1.8	1.7	2.0	238	236	240	4.0	283	-	-
Atg-serpentinite											
M14	8.0	-	-	-	-	-	-	-	-	1.8	340
M15	7.1	-	-	-	-	-	-	-	-	1.8	409
M51	8.3	-	-	-	-	-	-	-	-	1.8	322

All $\delta^{18}O$ values are given in SMOW. (*value*): duplicate; 1: thermometer serpentine/fluid of Saccocia et al (2009); 2: thermometer serpentine/magnetite of Wenner and Taylor (1971) revised by Früh-Green et al. (1996); *fluid value from Mottl et al. (2003).

AppendixA

Click here to download Background dataset for online publication only: AppendixA.docx

AppendixB

Click here to download Background dataset for online publication only: AppendixB.xlsx

AppendixC

Click here to download Background dataset for online publication only: AppendixC.xlsx

AppendixD

Click here to download Background dataset for online publication only: AppendixD.docx

AppendixE

Click here to download Background dataset for online publication only: Appendix E.xlsx

AppendixF

Click here to download Background dataset for online publication only: AppendixF.xlsx